AWARE

The Atmospheric Radiation Measurement (ARM) West Antarctic Radiation Experiment

Dan Lubin, Damao Zhang, Israel Silber, Ryan C. Scott, Petros Kalogeras,
Alessandro Battaglia, David H. Bromwich, Maria Cadeddu, Edwin Eloranta,
Ann Fridlind, Amanda Frossard, Keith M. Hines, Stefan Kneifel,
W. Richard Leaitch, Wuyin Lin, Julien Nicolas, Heath Powers,
Patricia K. Quinn, Penny Rowe, Lynn M. Russell, Sangeeta Sharma,
Johannes Verlinde, and Andrew M. Vogelmann

ABSTRACT: The U.S. Department of Energy Atmospheric Radiation Measurement (ARM) West Antarctic Radiation Experiment (AWARE) performed comprehensive meteorological and aerosol measurements and ground-based atmospheric remote sensing at two Antarctic stations using the most advanced instrumentation available. A suite of cloud research radars, lidars, spectral and broadband radiometers, aerosol chemical and microphysical sampling equipment, and meteorological instrumentation was deployed at McMurdo Station on Ross Island from December 2015 through December 2016. A smaller suite of radiometers and meteorological equipment, including radiosondes optimized for surface energy budget measurement, was deployed on the West Antarctic Ice Sheet between 4 December 2015 and 17 January 2016. AWARE provided Antarctic atmospheric data comparable to several well-instrumented high Arctic sites that have operated for many years and that reveal numerous contrasts with the Arctic in aerosol and cloud microphysical properties. These include persistent differences in liquid cloud occurrence, cloud height, and cloud thickness. Antarctic aerosol properties are also quite different from the Arctic in both seasonal cycle and composition, due to the continent's isolation from lower latitudes by Southern Ocean storm tracks. Antarctic aerosol number and mass concentrations are not only non-negligible but perhaps play a more important role than previously recognized because of the higher sensitivities of clouds at the very low concentrations caused by the large-scale dynamical isolation. Antarctic aerosol chemical composition, particularly organic components, has implications for local cloud microphysics. The AWARE dataset, fully available online in the ARM Program data archive, offers numerous case studies for unique and rigorous evaluation of mixed-phase cloud parameterization in climate models.

AFFILIATIONS: **Lubin and Russell**—Scripps Institution of Oceanography, La Jolla, California; **Scott**—NASA Langley Research Center, Hampton, Virginia; **Zhang, Lin, and Vogelmann**—Brookhaven National Laboratory, Upton, New York; **Silber and Verlinde**—The Pennsylvania State University, University Park, Pennsylvania; **Kalogeras and Battaglia**—University of Leicester, Leicester, United Kingdom; **Bromwich and Hines**—Byrd Polar and Climate Research Center, Columbus, Ohio; **Cadeddu**—Argonne National Laboratory, Lemont, Illinois; **Eloranta**—University of Wisconsin–Madison, Madison, Wisconsin; **Fridlind**—NASA Goddard Institute for Space Studies, New York, New York; **Frossard**—The University of Georgia, Athens, Georgia; **Kneifel**—University of Cologne, Cologne, Germany; **Leaitch and Sharma**—Environment and Climate Change Canada, Toronto, Canada; **Nicolas**—European Centre for Medium-Range Weather Forecasts, Reading, United Kingdom; **Powers**—Los Alamos National Laboratory, Los Alamos, New Mexico; **Quinn**—NOAA/Pacific Marine Environmental Laboratory, Seattle, Washington; **Rowe**—NorthWest Research Associates, Redmond, Washington, and University of Santiago, Santiago, Chile

W est Antarctica is one of the most rapidly warming regions on Earth, and this warming is closely connected with global sea level rise. The discovery of rapid climate change on the West Antarctic Ice Sheet (WAIS) has challenged previous explanations of Antarctic climate change that focused on strengthening of circumpolar westerlies in response to the positive polarity trend in the southern annular mode (Bromwich et al. 2013; Nicolas and Bromwich 2014). West Antarctic warming trends do not yet have a comprehensive explanation. Dynamical mechanisms may vary from one season to the next, and these mechanisms very likely involve complex teleconnections with subtropical and tropical latitudes (e.g., Ding et al. 2011; Schneider et al. 2012). Field work for atmospheric and climate science has historically been sparse due to logistical challenges (Bromwich et al. 2012), especially for West Antarctica, where the areas of greatest interest for sea level rise are very distant from the major or permanent field stations of any nation's Antarctic program. Direct meteorological information on the WAIS has mostly been limited to a few automatic weather stations (AWS) for several decades (Lazzara et al. 2012). And yet satellite imagery, measurements, and meteorological reanalyses indicate that West Antarctica is highly susceptible to advection of warm and moist maritime air, with related cloud cover, depending on the location and strength of low pressure centers in the Amundsen, Ross, and Bellingshausen Seas (Jolly et al. 2018; Nicolas and Bromwich 2011). At the same time, satellite profiling, even with active sensors, often misses important details regarding clouds and precipitation in the Antarctic lower troposphere (e.g., Maahn et al. 2014), and this further emphasizes the need for comprehensive surface-based measurements. Recently, Scott et al. (2019) have linked surface melting conditions on the WAIS to blocking activity in the Amundsen Sea region and to a negative phase of the southern annular mode, both of which correlate with El Niño conditions in the tropical Pacific Ocean. There is a need to quantify the role of these changing air masses on the surface energy balance (SEB), including all surface energy components and cloud radiative forcing (e.g., Bromwich et al. 2012; Trenberth and Fasullo 2010; Hyder et al. 2018; Silber et al. 2019a). More generally, global climate model simulations are known to perform poorly over the Antarctic and Southern Ocean (e.g., Trenberth and Fasullo 2010; Hyder et al. 2018), and the relative scarcity of cloud information at southern high latitudes has so far inhibited progress.

Surface melt conditions during summer are increasingly realized to have a potentially important role in WAIS mass loss. Analysis of satellite and aerial photographic observations by Kingslake et al. (2017) reveals how extensively and frequently surface melt conditions can occur throughout lower-elevation regions of Antarctica. The largest immediate cause of ice sheet acceleration in West Antarctica is recognized to be ice shelf thinning via basal melting from a

warming ocean (Pritchard et al. 2012; Paolo et al. 2015). Concurrent with this ocean-induced ice shelf loss is retreat of the grounding line (the transition between the ice sheet and floating ice shelf) throughout West Antarctica (Rignot et al. 2014). Once stabilization by ice shelf buttressing is lost (Fürst et al. 2016), ice sheet acceleration in West Antarctica is potentially rapid due to the underlying topography that slopes downward as one goes inland. This is the well-known marine ice sheet instability (MISI; Weertman 1974; Oppenheimer 1998; Alley et al. 2015). A MISI-related collapse may have already started for the Thwaites Glacier basin (Joughin et al. 2014).

However, the major role of oceanic warming in West Antarctica does not signify that direct atmospheric warming is a negligible factor. Pollard et al. (2015) and DeConto and Pollard (2016) have identified a marine ice cliff instability (MICI) that operates in conjunction with the MISI. When surface air temperatures approach and exceed freezing, surface meltwater filtering into crevasses can induce hydrofracturing near the grounding line, weakening the grounded ice column at its edge and increasing the calving rate (see also Bassis and Jacobs 2013). Hydrofracturing will also occur on the ice shelves themselves, further increasing their loss rate and exposing these unstable ice cliffs at the grounding line (DeConto and Pollard 2016). The three overarching processes in cryosphere mass loss are direct melt runoff, glacier and ice sheet calving, and ice shelf ablation through basal melting. The difference between the net of these processes and accumulation defines the mass balance of the cryosphere (Zwally et al. 2005). These three processes are also interrelated. For example, on grounded ice sheets, meltwater can accelerate ice sheet motion and calving by 1) filtering down to the base of the ice sheet and lubricating its downslope motion and 2) hydrofracturing, in which surface meltwater ponds and infiltrates crevasses, acting as a slow-motion "jackhammer" that weakens an ice shelf structure (e.g., Scambos et al. 2000).

All three of these processes play important roles in Greenland (e.g., Fürst et al. 2015). In Antarctica, we are mainly concerned about the stability of systems of moving ice sheets partially buttressed by their adjacent and attached floating ice shelves. Fürst et al. (2016) demonstrate that ice shelf buttressing plays a critical role in the stability of ice sheets adjacent to the Amundsen and Bellingshausen Seas. Moreover, the recent work of Pollard et al. (2015) and DeConto and Pollard (2016) indicates an important role for direct atmospheric forcing on ice shelf hydrofracturing in West Antarctica. Parameterizations for ice shelf hydrofracturing and the MICI in coupled climate models are still in their early stages; actual field data are required for model testing and refinement, and for attribution of surface melting events to specific atmospheric processes such as warm air intrusion (Nicolas and Bromwich 2011; Scott et al. 2019), cloud all-wave surface radiation enhancement (Bennartz et al. 2013; Hu et al. 2019), or foehn winds (e.g., Elvidge et al. 2015; Zou et al. 2019).

AWARE is an effort to acquire critical atmospheric data to fundamentally understand atmospheric forcing on West Antarctica, and to foster related improvements to climate model performance. Within the past two decades other regions of the Antarctic continent have seen several field campaigns and growing permanent installations of advanced atmospheric science equipment, all of which are providing new insights into the continent's unique meteorology and climatology. Two of the most persistent efforts have occurred on the high plateau of East Antarctica: 1) at the South Pole with Fourier transform infrared (FTIR) spectroradiometer measurements (e.g., Walden et al. 2006; Town et al. 2007), and micropulse lidar (MPL) combined with tethered balloon cloud microphysical observations (Lawson and Gettelman 2014), and 2) multisensor observations of ice clouds over Dome C that include multispectral microwave radiometry (Ricaud et al. 2017). Research radars for cloud and precipitation recently deployed at Dumont d'Urville Station in Adélie Land have revealed how katabatic outflows sublimate precipitation, thus impacting the long-term ice mass balance (Grazioli et al. 2017). A climate observatory has been established at Princess Elizabeth Base in Queen Maud Land, East Antarctica, that presently maintains a precipitation radar along with comprehensive

meteorological measurements whose combined data enable studies of both cloud microphysics and surface mass balance (Gorodetskaya et al. 2015). The British Antarctic Survey's Rothera Station, in the southern Antarctic Peninsula region, serves as a base for aircraft-based in situ cloud microphysical observations that have revealed details about warm-temperature secondary ice production in Antarctic clouds (Lachlan-Cope et al. 2016). West Antarctica, due to its extreme remoteness, has yet to see a permanent installation of atmospheric or climate science instrumentation beyond AWS (Lazzara et al. 2012), but the AWARE campaign has made a start. Figure 1 shows the location of the two AWARE deployments. Within the entire sector of Antarctica shown in this figure, only four locations (indicated by red markers) have seen atmospheric and climate science experiments using modern instrumentation with multiple sensors: McMurdo Station and its immediate surroundings on and near the western Ross Ice Shelf (RIS), South Pole Station, WAIS Divide Ice Camp, and Rothera Station.

This report on the AWARE campaign is organized with three scientific motivations. The first is to illustrate contrasts between the Antarctic and the relatively better-observed Arctic. The high Arctic is a partially frozen ocean surrounded by continental landmasses, with one major ice sheet (Greenland) contributing to sea level rise. The Arctic radiation budget is strongly influenced by persistent and long-lived mixed-phase clouds (e.g., Morrison et al. 2012; Bennartz et al. 2013). High southern latitudes are characterized by a continent with greatly varying topography at high elevations surrounded by the world's most turbulent ocean. The SEB at the vulnerable extremities of Antarctic ice sheets is influenced on one hand by katabatic and topographic influences on atmospheric dynamics and cloud physics, and on the other hand by adjacent Southern Ocean storm tracks (Nicolas and Bromwich 2011) that are in turn influenced by teleconnections with lower latitudes. The more varied influences on Antarctic clouds often yield markedly different manifestations of mixed-phase cloud microphysics than seen in the Arctic (Scott and Lubin 2016).
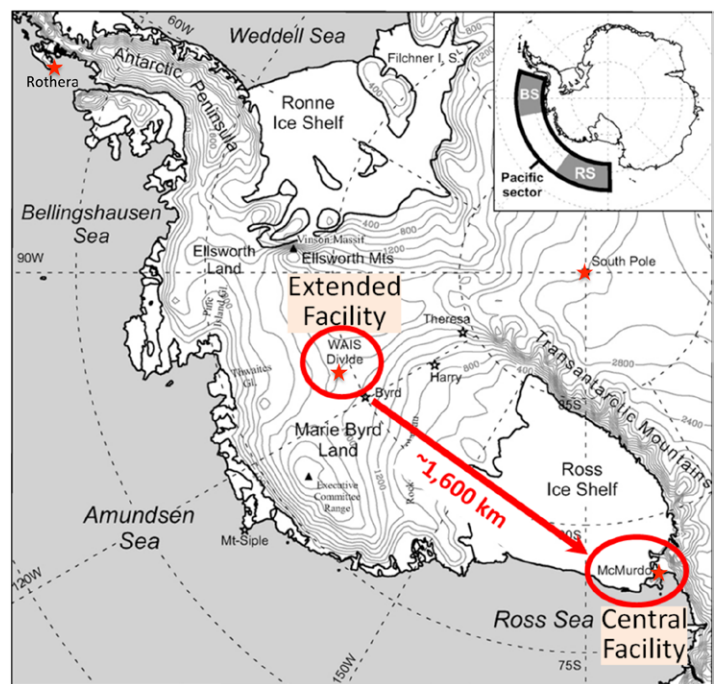
A second motivation is the need to keep

Fig. 1. Map of West Antarctica, the Transantarctic Mountains, and the Ross Ice Shelf, showing the AWARE measurement locations at McMurdo Station and the WAIS Divide Ice Camp. The insert at the upper right indicates maritime regions Ross Sea (RS) and Bellingshausen Sea (BS) that influence moisture advection/cloud and clear skies over West Antarctica, respectively. Adapted from Nicolas and Bromwich (2011).

aerosol chemistry and microphysics on an equal footing with meteorology and cloud microphysics. The study of aerosol–cloud interaction has become inseparable from any thorough and current study of mixed-phase cloud life cycle, and our presentation of contrasts between the Antarctic and the Arctic must necessarily include aerosol climatology. Finally, we demonstrate how AWARE data from West Antarctica can be used to evaluate performance of both regional and climate models, in the region where atmospheric warming is expected to exacerbate ice shelf loss and Antarctic contribution to sea level rise.

Experiment design

AWARE deployed the second ARM Mobile Facility (AMF) to McMurdo Station on Ross Island, Antarctica, to sample an annual cycle in atmospheric structure and thermodynamics, surface

radiation budget and cloud properties. The ARM Mobile Facility deployments began in 2005 in response to the substantial success that the three fixed ARM sites realized for gathering advanced atmospheric sensor data for climate model development and validation (Mather and Voyles 2013). The AMFs consist of cloud research radars, lidars, multiple broadband and spectral radiometers, an aerosol observation suite, and thorough meteorological sampling ranging from surface turbulent flux equipment to radiosondes. The AMFs are intended to address key issues in atmospheric science by deploying the entire multisensor suite to a given location for at least several months of data collection, thereby making a substantial advance in the field.

In October 2013 the AWARE campaign, organized by researchers from the Scripps Institution of Oceanography (SIO), Byrd Polar and Climate Research Center (BPCRC), The Pennsylvania State University, and Brookhaven National Laboratory (BNL), was awarded the use of the second Mobile Facility (AMF2) to address the current concerns related to Antarctic climatic warming discussed above. Transportation, construction and power requirements of an AMF necessitated the choice of McMurdo Station as the site for the full AMF deployment. At the same time, the ARM Program recognized the value in collecting data directly from West Antarctica, and the AWARE campaign was fortunate to be awarded a second and smaller suite of instruments optimized for SEB measurement for deployment at one of the summer-only field stations in West Antarctica.

McMurdo Station (77°50′47″S, 166°40′06″E) is generally a challenging location for meteorological and aerosol sampling because of complex terrain variability and related microclimates including rapidly shifting wind direction. The CosRay location 1 km from McMurdo (Fig. 2) provided the research radars with a clear view across an open fetch of water in southeasterly through southwesterly directions, which are the prevailing wind directions. The WAIS Divide Ice Camp (WAIS Divide; 79°28′03″S, 112°05′11″W; elevation: 1797 m) was chosen as the most logistically suitable station for the SEB measurement suite, based on power and transportation constraints. The U.S. Antarctic Program (USAP) allocated the AWARE campaign's extended facility component (Fig. 1) one LC-130 aircraft mission to transport to WAIS Divide all personnel and equipment, including laboratory housing (half-size sea container) and helium for radiosondes. The extremely flat and even terrain at WAIS Divide offered an ideal site for radiometry and SEB measurement, with the largest instrumental challenge being optical obstruction and occasional instrument fouling
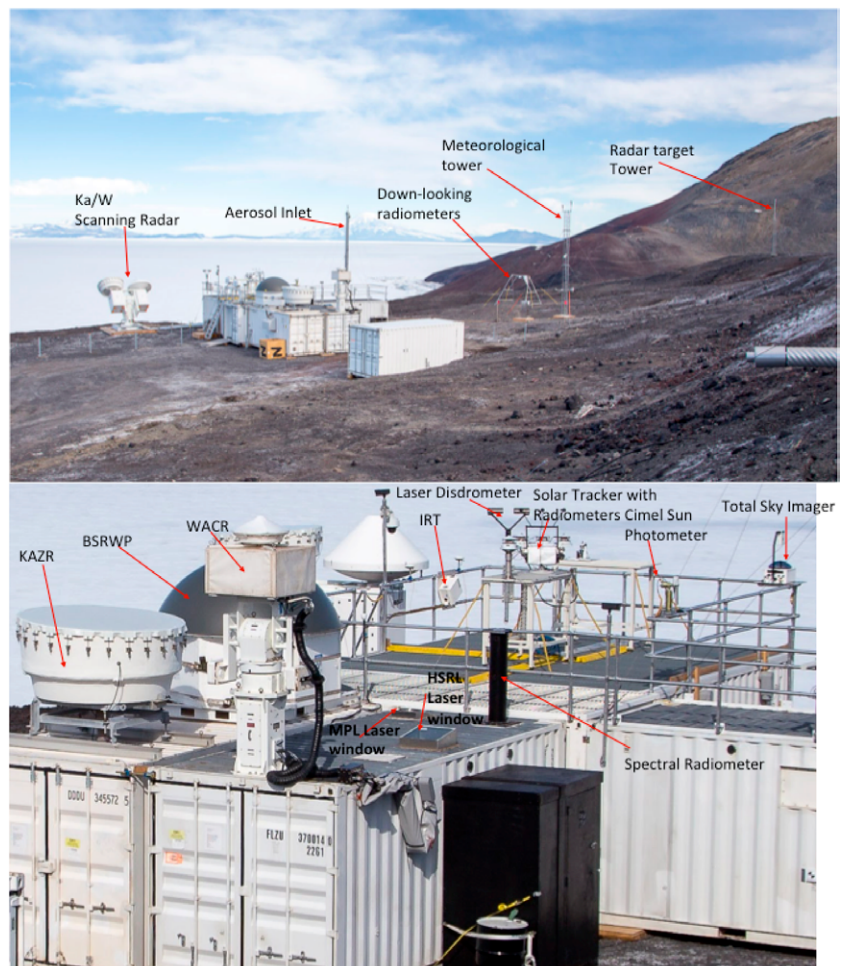

Fig. 2. The AMF2 installation at the McMurdo Station CosRay site. (top) View of the entire site showing locations of adjacent meteorological and radar calibration target towers, and the southerly view of the scanning radars. (bottom) Detail of instrument installation within the AMF2.

during extended periods of strong winds and blowing snow. Figure 3 shows the sea container installation at WAIS Divide. Table 1 lists the AMF2 instruments at CosRay and Table 2 lists the instruments deployed to WAIS Divide. These tables also provide the instrument acronyms used in the text. At McMurdo Station the AMF2 began full operation on 1 December 2015, with some instruments operating earlier, and continued through 31 December 2016. At WAIS Divide, the AWARE instruments began operation with sondes on 4 December 2015, with all instruments operating by 7 December and continuing until 17 January 2016.

In the following sections we demonstrate how climatological information on cloud properties is derived from the AMF2 measurements, and we discuss contrasts with cloud properties obtained from Arctic locations with nearly identical instrumentation. We also discuss AMF2 case studies suitable for model evaluation, again contrasting AWARE retrievals from their Arctic counterparts. We
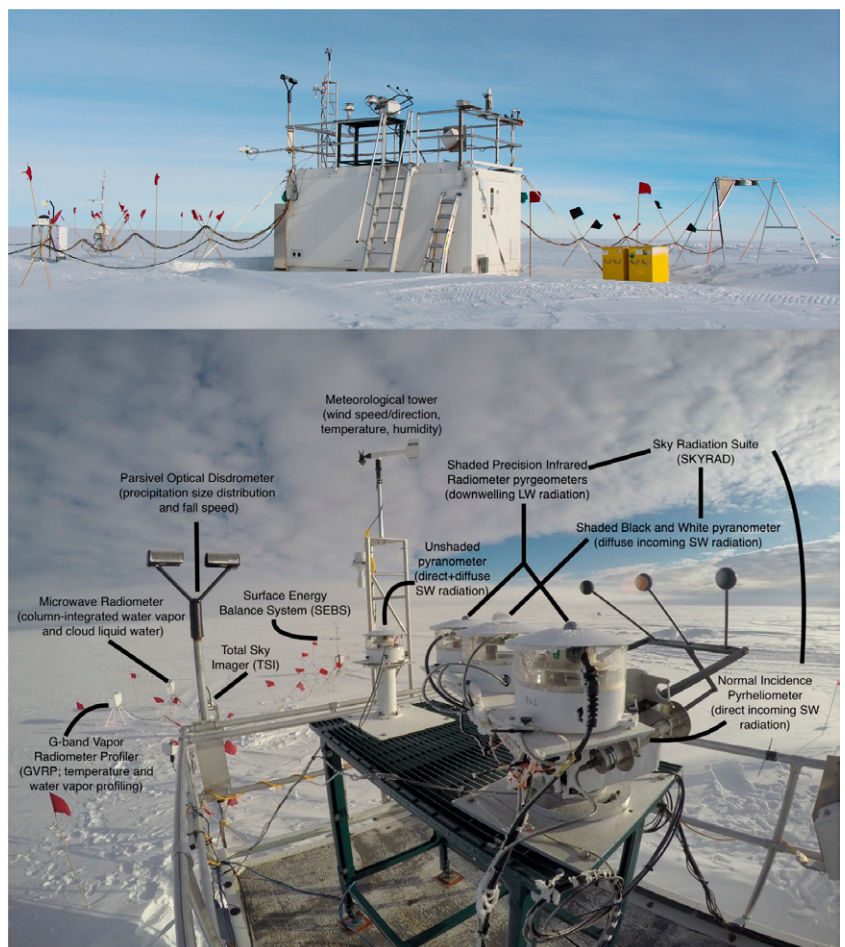

Fig. 3. The AWARE surface energy budget equipment at WAIS Divide. (top) View of the sea container housing most of the instruments, with the SKYRAD installation at the far right and Total Sky Imager, ceilometer, and surface turbulent flux instruments at the far left. (bottom) Detail of the instrument installation on the roof of the sea container.

then illustrate how the WAIS Divide dataset can be used as a case study for both regional and global climate model evaluation regarding cloud microphysics. At WAIS Divide AWARE was fortunate to sample the edge of a surface melt event that spanned a third of West Antarctica and most of the RIS and lasted from 10 to 18 January 2016 at WAIS Divide (Nicolas et al. 2017). The rapid transition between climatologically typical summer conditions and the much warmer conditions of the melt onset represents a step function that provides a stringent test of microphysical parameterization performance in response to the changing model input fields (e.g., Wilson et al. 2018).

Preliminary instrumental results and Arctic comparison
Climatological comparisons. Silber et al. (2018a,b, 2019a) have developed a multisensor approach to determine key climatological cloud properties from high-latitude ARM data, including occurrence fraction, cloud persistence and boundaries, and cloud location relative to temperature and moisture inversions. In the application of this approach at McMurdo, Ka-band ARM zenith radar (KAZR) data from both general and moderate sensitivity operating modes are used for hydrometeor detection throughout the troposphere, similar to Clothiaux et al. (2001), and these detections are gridded to the High Spectral Resolution Lidar (HSRL) 7.5-m vertical resolution and 30-s time sampling. HSRL data are then used to refine the cloud detection process by analyzing the log-scaled particulate backscatter cross section β_p as a function of the linear

depolarization ratio (LDR). Different regions in the scatter diagram of β_p versus LDR correspond to liquid water droplets, cloud ice particles, or aerosol particles, and the observational occurrence in each of these regions provides climatological information as a function of altitude.

Table 1. Instruments deployed to Ross Island (McMurdo Station CosRay site). Instruments marked with an asterisk are deployed first at WAIS Divide December 2015–January 2016 and then redeployed to CosRay for the remainder of the field program.

Instrument name	Instrument acronym	Quantities measured
X-band and Ka-band scanning ARM cloud radar	X/KA-SACR	Co- and cross-polar radar Doppler spectrum and moments (reflectivity, Doppler velocity, spectrum width, linear depolarization ratio, differential reflectivity)
Scanning W-band ARM cloud radar	SWACR	Radar Doppler spectrum and moments
Ka-band ARM zenith radar	KAZR	Radar Doppler spectrum and moments at high (30-m) range resolution
Atmospheric Emitted Radiance Interferometer	AERI	Absolute thermal infrared spectral radiance emitted by the atmosphere down to the instrument
High-spectral-resolution lidar	HSRL	Aerosol optical depth, volume backscatter, cross section, cloud and aerosol depolarization
Micropulse lidar	MPL	Altitude of cloud layers
Vaisala ceilometer	VCEIL	Cloud-base height
Beam-steerable radar wind profiler	RWP	Wind and virtual temperature profiles
Parsivel optical disdrometer	PARSIVEL	Precipitation particle size distribution and fall speed
Cloud condensation nuclei counter	CCN	Cloud condensation nuclei as function of supersaturation
Condensation particle counter	CPC	Total aerosol particle concentration down to diameter 10 nm
Hygroscopic tandem differential mobility analyzer	HTDMA	Aerosol size, mass, or number distribution as function of RH
Ambient nephelometer	NEPH AMB	Aerosol light scattering coefficient at ambient RH
Dry nephelometer	NEPH DRY	Dry aerosol light scattering coefficient
Ozone	O_3	Ozone concentration
Particle soot absorption photometer	PSAP	Optical transmittance of aerosol particles
Aerosol filter sampling (SIO)	AER FLTR	Aerosol chemical composition by FTIR and XRF
Upward-looking precision spectral pyranometer	SKYRAD PSP	Downwelling total shortwave irradiance
Upward-looking Eppley model 8–48 diffuse pyranometer	SKYRAD 8–48	Downwelling diffuse shortwave irradiance
Upward-looking precision infrared radiometer	SKYRAD PIR	Downwelling longwave irradiance
Upward-looking infrared thermometer	SKYRAD IRT	Sky equivalent blackbody temperature
Downward-looking precision spectral pyranometer	GRNDRAD PSP	Upwelling shortwave radiation reflected by surface
Downward-looking precision infrared radiometer	GRNDRAD PIR	Upwelling longwave radiation emitted by surface
Downward-looking Infrared thermometer	GRNDRAD IRT	Surface equivalent blackbody temperature
Cimel sunphotometer	CSPHOT	Multispectral direct solar irradiances
Multifilter rotating shadowband radiometer	MFRSR	Direct normal, diffuse horizontal, and total horizontal irradiances at six standard wavelengths
Analytical Spectral Devices FieldSpec Pro shortwave spectroradiometer (SIO)*	ASD*	Downwelling spectral shortwave irradiance 350–2200 nm
Eddy correlation flux measurement system	ECOR	Surface turbulent fluxes of momentum, sensible heat, latent heat, and carbon dioxide
Total sky imager	TSI	Cloud fraction
Vaisala present weather detector	PWD	Visibility, precipitation detection
G-band vapor radiometer*	GVRP*	High-time-resolution water vapor and temperature profiling, and column-integrated liquid water and water vapor
Microwave radiometer, two channel	MWR, 2C	Column-integrated liquid water and water vapor
Balloon-borne sounding system	SONDE	Vertical profiles of T, P, RH, wind speed and direction
Meteorological instrumentation at AMF	MET	Near-surface (2-m) T, P, RH, wind speed and direction
Local meteorology at top of AOS stack	AOS MET	Wind speed, direction, T, RH, P

Table 2. Instruments deployed to the WAIS Divide Ice Camp.

Instrument name	Instrument acronym	Quantities measured
Upward-looking precision spectral pyranometer	SKYRAD PSP	Downwelling total shortwave irradiance
Upward-looking Eppley model 8–48 diffuse pyranometer	SKYRAD 8–48	Downwelling diffuse shortwave irradiance
Upward-looking precision infrared radiometer	SKYRAD PIR	Downwelling longwave irradiance
Upward-looking infrared thermometer	SKYRAD IRT	Sky equivalent blackbody temperature
Downward-looking precision spectral pyranometer	GRNDRAD PSP	Upwelling shortwave radiation reflected by surface
Downward-looking precision infrared radiometer	GRNDRAD PIR	Upwelling longwave radiation emitted by surface
Downward-looking Infrared thermometer	GRNDRAD IRT	Surface equivalent blackbody temperature
Cimel sunphotometer	CSPHOT	Multispectral direct solar irradiances
Multifilter rotating shadowband radiometer	MFRSR	Direct normal, diffuse horizontal, and total horizontal irradiances at six standard wavelengths
Analytical Spectral Devices FieldSpec Pro shortwave spectroradiometer (SIO)	ASD	Downwelling spectral shortwave irradiance, 350–2200 nm (Lubin)
Eddy correlation flux measurement system	ECOR	Surface turbulent fluxes of momentum, sensible heat, latent heat, and carbon dioxide
Total sky imager	TSI	Cloud fraction
Vaisala ceilometer	VCEIL	Cloud base height
Parsivel optical disdrometer	PARSIVEL	Precipitation particle size distribution and fall speed
Vaisala present weather detector	PWD	Visibility, precipitation detection
G-band vapor radiometer	GVRP	High-time-resolution water vapor and temperature profiling, and column-integrated liquid water and water vapor
Microwave radiometer, two channel	MWR, 2C	Column-integrated liquid water and water vapor
Balloon-borne sounding system	SONDE	Vertical profiles of T, P, RH, wind speed and direction
Meteorological instrumentation at AMF	MET	Near-surface (2 m) T, P, RH, wind speed and direction

The multisensor approach used here is optimized for polar regions. The liquid water cloud-base-height algorithm in Silber et al. (2018b) differs from earlier ARM retrievals in that it is optimized for detection of a polar cloud base, as opposed to any cloud base (e.g., as in ceilometer algorithms). This algorithm uses the backscatter cross section's first and second derivatives to accurately determine the cloud base height. The hydrometeor detection algorithm described in Silber et al. (2018a, 2019a) using lidar is based on identifying local minima in monthly histograms of backscatter versus LDR, such that no fixed backscatter and/or LDR thresholds for liquid or ice are used, but instead, adaptive-dependent thresholds may vary in time, thereby reducing error in phase classification. Hydrometeor detection using KAZR as describe in Silber et al. (2018a) is based on a signal-to-noise ratio (SNR) threshold but is otherwise not significantly different than earlier ARM retrieval methods.

This multisensor approach is applied here to both McMurdo AMF2 and ARM North Slope of Alaska (NSA) data, with climatological contrasts demonstrated in Figs. 4–7. The NSA site is located at Utqiaġvik (71.3°N, 156.8°W; formerly referred to as Barrow, Alaska), adjacent to the Beaufort Sea, and is representative of an Arctic maritime location with variable sea ice concentration. Instrumentation at the NSA site is very similar to the AMF2 deployed at McMurdo, and the ARM data reduction and quality-control pipeline is identical for the two sites (Peppler et al. 2008). The NSA data analysis presented here is based on measurements from 2015, which correspond with previous analyses of longer datasets from this site (e.g., Shupe 2011).

Figure 4 shows 30-day running-mean total hydrometeor and liquid-cloud occurrence fractions at McMurdo and NSA over an annual cycle. The total duration is 721 h, and an

odd hour number was required for the smoothing to center the data properly, hence the indication of plus 1 h in the caption. The temperature curve, based on radiosonde profiles, represents the average temperature between the surface and 4-km altitude. We see that the annual hydrometeor (liquid) occurrence fraction is higher by ~20% (~31%) at NSA relative to McMurdo. Figure 5 shows seasonal averages of cloud thickness, highest cloud-top height and highest cloud-top temperature. Here the highest cloud-top height is the highest bin with any detected hydrometeor using the combined HSRL and KAZR method of Silber et al. (2018b), and the highest cloud-top temperature is the corresponding temperature computed from the sonde data linearly interpolated in time. Most clouds are thicker at McMurdo relative to NSA, but the deepest, likely frontal, clouds are observed at NSA. The annual highest cloud-top heights

Fig. 4. The 30-day (+1-h) running-mean total hydrometeor and liquid-cloud occurrence fractions at McMurdo (solid) and Utqiaġvik (dashed). The monthly mean values are given by the filled markers. The months represented in each season here for McMurdo (Utqiaġvik) are DJF (JJA) for summer, MAM (SON) for autumn, JJA (DJF) for winter, and SON (MAM) for spring. The temperature curve (based on sounding profiles) represents the average temperature between the surface and 4-km altitude. The x axis ticks mark the sixteenth of each month at 0000 UTC. The annual hydrometeor (liquid) occurrence fraction is higher by ~20% (~31%) at Utqiaġvik relative to McMurdo.

are more variable at NSA but generally comparable at both sites (both having elevation close to sea level), while the highest cloud-top temperatures are mostly lower and less variable at McMurdo.

Figure 6 provides similar seasonal averages of total cloud and liquid-bearing layer persistence. Liquid-cloud layers are significantly more persistent at NSA than McMurdo, a result likely influenced by 1) the complex topography and lack of significant moisture sources at McMurdo relative to NSA (Monaghan et al. 2005), and 2) synoptic flow and advection being different for the two sites. While the longest-lived layers are observed in summer at NSA, McMurdo exhibits different seasonal behavior (depending on the examined percentile). Figure 7 illustrates the seasonal variability of the lowest liquid-bearing cloud layer base height, as well as its annual cumulative distribution function. The lowest liquid-bearing cloud layers are significantly higher at McMurdo relative to NSA, but liquid is detected at higher altitudes at NSA, due to typically warmer temperatures in the atmospheric profile (Fig. 5). These cloud layers are evenly distributed up to ~3 km at McMurdo while over NSA, they are mostly concentrated near the surface.

Statistical significance of the comparisons between McMurdo and Utqiaġvik in Figs. 4–7 was assessed using a two-sample Kolmogorov–Smirnov test at the 95% confidence level, to determine if the samples represent different variable distributions. The distributions were found to be different at this confidence level for all retrievals in Figs. 4, 5, and 7, and for liquid water clouds during spring in Fig. 6.

The distribution of aerosol particles in the Antarctic is characterized by its unique location and surrounding ocean (which largely isolates it from the sources present on other continents), its near-complete coverage by ice and snow (which eliminates most local non-sea-salt-dust and terrestrial biological particle sources), and its near-absence of human activities (which minimizes the emissions from combustion, cooking, and other human activities). The lack
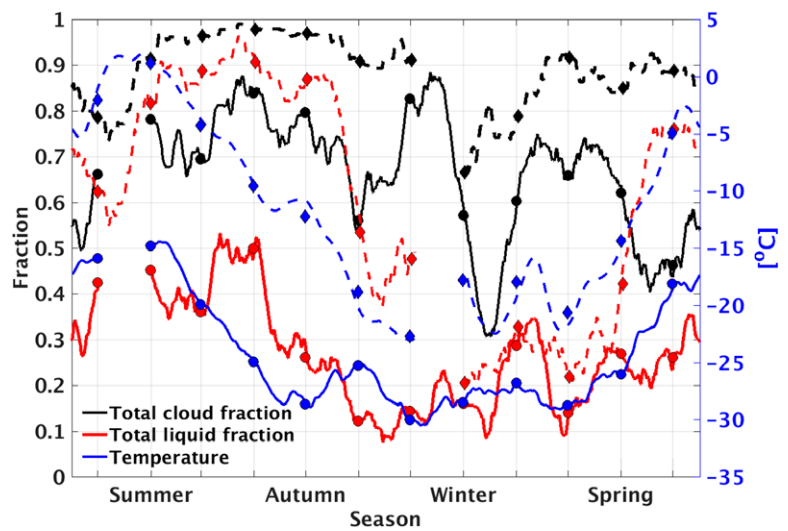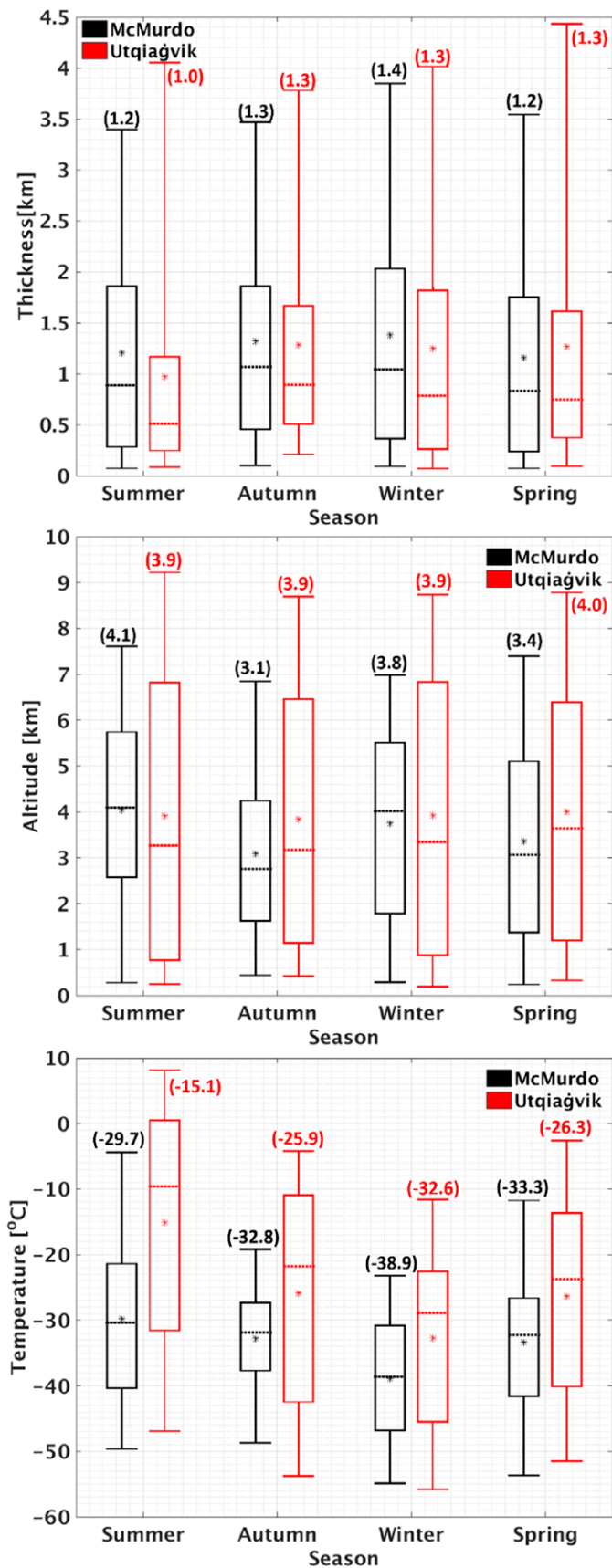
Fig. 5. Box-and-whisker diagrams of (top) cloud (hydrometeor) thickness, (middle) highest cloud-top height, and (bottom) highest cloud-top temperature, designating the median (thick dotted line), 1st and 3rd quartiles (box edges), 5th and 95th percentiles (whiskers), and mean (asterisk; values are provided in the parentheses).
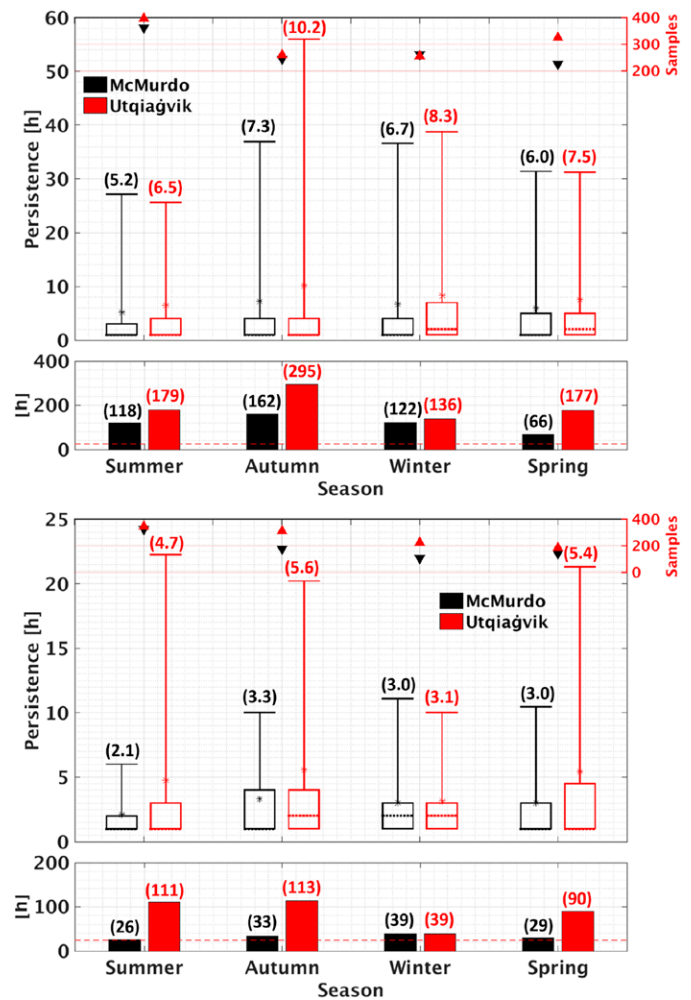

Fig. 6. Box-and-whisker diagram of (top) cloud and (bottom) liquid-bearing layer persistence. The total numbers of cloud (liquid) samples in each month are shown by the triangle markers. The bars represent the longest-lived liquid-bearing cloud layers observed in each season (values are provided in the parentheses; dashed red line denotes 24 h).

of orographic features in the Southern Ocean surrounding Antarctica supports the midlatitude westerlies, effectively defying substantial transport of continental emissions into the Antarctic region. The result is that aerosol concentrations reflect the seasonal trends of ocean phytoplankton (non-sea-salt sulfate), seabirds (organic mass), wind-driven sea spray (salt), and non–sea salt dust, as is shown in Fig. 8b.

The OM concentration is highest in summer during AWARE, when seabird activity is also high. The breakdown products of urea deposits from seabirds result in a variety of organic products in the vapor phase (Legrand et al. 2012), some of which
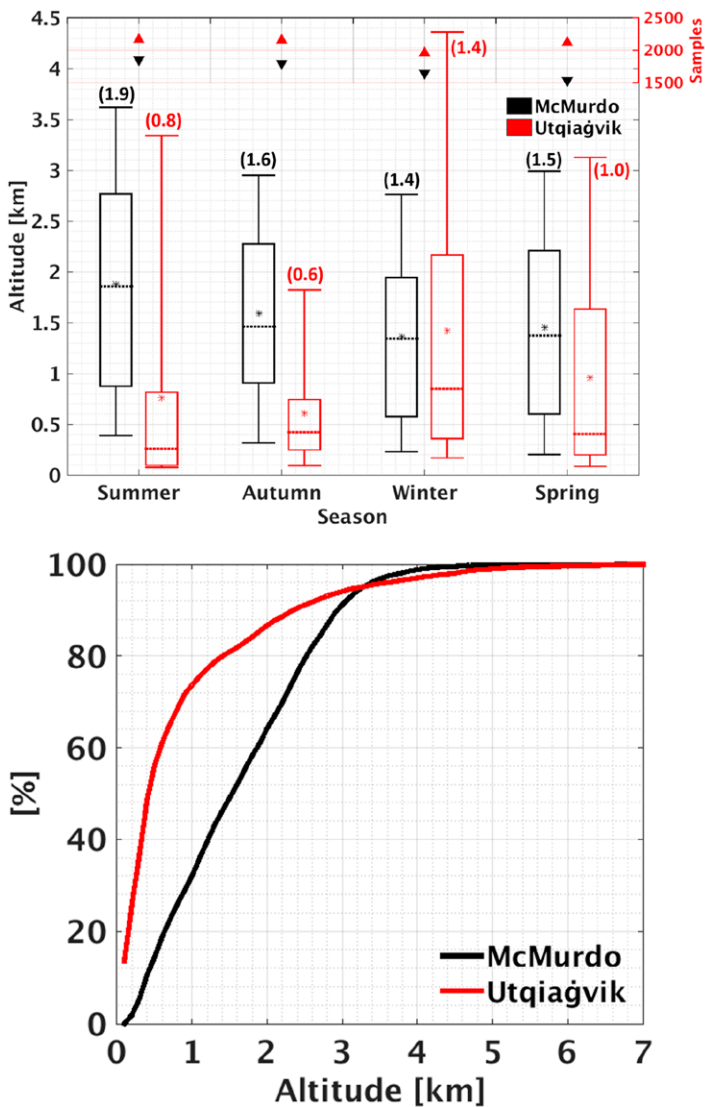
Fig. 7. (top) Lowest (per profile) liquid-bearing cloud-layer base height box-and-whisker diagram and (bottom) annual cumulative distribution function.

condense and, along with ammonia (Legrand et al. 1998), contribute to particle-phase ammonium and OM. Of course human activities at McMurdo Station, while minimal compared to those of urban regions, also contribute OM, but in the summer that accounts for less than half of the observed OM (Fig. 3 of Liu et al. 2018). Some OM may also be associated with the submicron salt from sea spray, but the FTIR spectroscopy spectra are more consistent with seabird sources (Schmale et al. 2013) and the seasonal trend of OM concentration is not consistent with an association with salt from sea spray (Liu et al. 2018). Even though the non–sea salt sulfate concentration tracks the OM closely, the strong summertime signature is likely attributable nearly entirely to a different source, namely, the production of DMS by ocean phytoplankton and subsequent oxidation to form non–sea salt sulfate. Submicron non–sea salt dust mass concentration is also highest in summer, likely as a result of both increased human activities and more exposed soil. During AWARE, the salt mass concentration is very small, with seasonal means and medians from 0.02 to 0.11 μg m^{-3} and maximum weekly values below 0.2 μg m^{-3} in winter. This cycle is driven by the local upwind wind speeds at the sea surface as well as the additional contributions of wind-driven frost flowers on new sea ice in winter (Liu et al. 2018).

In Fig. 9 we present data from two Arctic sites for comparison with AWARE. Figure 10 provides seasonal statistics comparing Utqiaġvik with AWARE. At the Alert Observatory (82.45°N, 62.51°W; Leaitch et al. 2018), the contributions from organic functional groups to the Arctic submicron aerosol were measured using 126 weekly integrated samples collected from April 2012 to October 2014. Routine outdoor high-volume samples of total suspended particles have been collected at Alert for inorganic chemical composition since 1980 (e.g., Barrie and Hoff 1985), and submicron sampling for inorganic ion analysis was started in March 2011. As a special study, weekly collections of particles smaller than 1 μm on Teflon filters were collected for FTIR spectroscopy of organic functional groups (OFG) from April 2012 to October 2014.

At Alert the cycle in salt mass concentration is similar to that of AWARE, with as much as 0.5 μg m^{-3} in winter and below 0.1 μg m^{-3} in summer (Fig. 9). At NSA the winter concentrations are higher with a mean of 1 and weekly averaged values of up to 2 μg m^{-3}, consistent with the closer proximity to seasonal new sea ice associated with higher frost flower frequency (Shaw et al. 2010; Xu et al. 2013, 2016). The evidence for Na depletion relative to Cl supports a wintertime contribution from frost flowers during AWARE (Liu et al. 2018), since the higher freezing temperature of Na salts relative to Cl salts indicates the role of wicking from brine pools in particle formation.
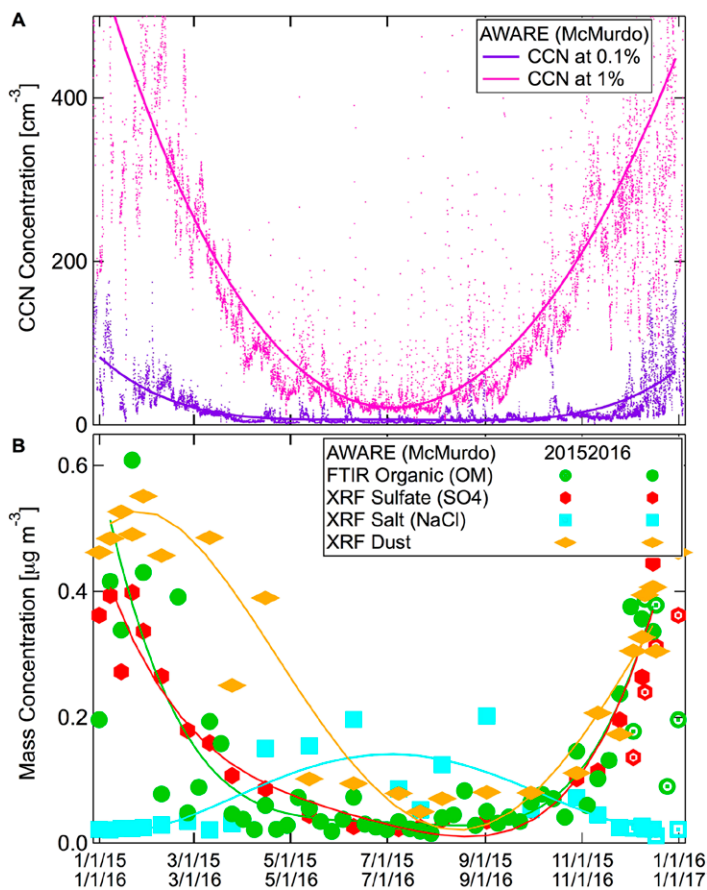
Fig. 8. CCN and submicron aerosol particle mass concentrations during annual cycles measured at McMurdo Station, Antarctic: (a) CCN at 0.1% and 1% supersaturation and (b) organic, non–sea salt sulfate (SO$_4$), sea salt, and non–sea salt dust mass concentration (from Liu et al. 2018). Sea salt particle mass concentration was estimated as the sum of measured Na*1.47 and Cl based on Bates et al. (2009), and non–sea salt sulfate (SO$_4^{2-}$) mass concentration was scaled from XRF *S* after removing for sea salt associated *S* (Liu et al. 2018). Non–sea salt dust mass concentration was calculated from XRF metal concentrations, assuming dust consists of MgCO$_3$, Al$_2$O$_3$, SiO$_2$, K$_2$O, CaCO$_3$, TiO$_2$, Fe$_2$O$_3$, MnO, and BaO after removing sea salt–associated metal amounts (Liu et al. 2018). Lines show five-parameter polynomial fits to 2016 measurements.
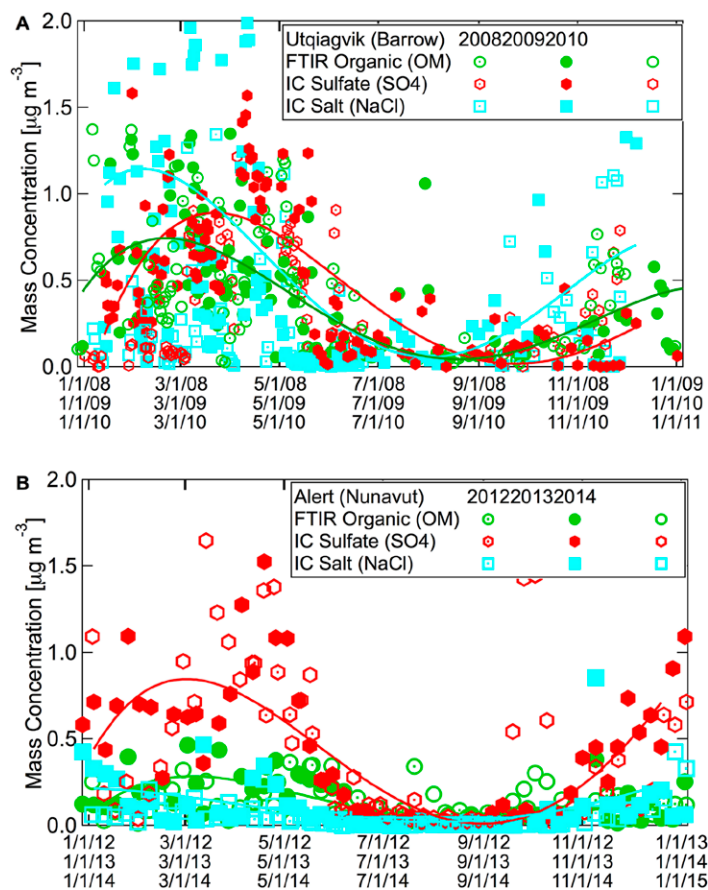
Fig. 9. Submicron aerosol particle mass concentrations during annual cycles for the Arctic: (a) organic, non–sea salt sulfate (SO$_4$), and sea salt mass concentration measured at Utqiaġvik, Alaska, by FTIR and IC (Shaw et al. 2010; Frossard et al. 2011; Quinn et al. 2002); (b) organic, non–sea salt sulfate (SO$_4$), and sea salt mass concentration measured at Alert, Nunavut, by FTIR and IC (Leaitch et al. 2018). Sea salt particle mass concentration was estimated as the sum of measured Na*1.47 and Cl based on Bates et al. (2012), and non–sea salt sulfate (SO$_4^{2-}$) mass concentration was calculated from IC sulfate after removing for sea salt associated SO4. Lines show five-parameter polynomial fits to 2009 (Utqiaġvik) and 2013 (Alert) measurements.

In contrast, the highest non–sea salt sulfate and organic mass concentrations in the annual cycles in the Arctic at both NSA and Alert show the well-known springtime haze that results from transport from the northern midlatitudes, as illustrated in Fig. 9 (Shaw 1982; Law and Stohl 2007; Quinn et al. 2007). The overall low concentrations of submicron mass concentration are otherwise a common feature of the Arctic and Antarctic. The Utqiaġvik sulfate mass concentration means and medians in winter and spring exceed those of summer and autumn by more than a factor of 2, obscuring any smaller differences that could be present for biological sources of non–sea salt sulfate between summer and winter seasons. Another interesting difference is the relative amount of non–sea salt sulfate to organic mass, which is nearly 1:1 in summer at AWARE and NSA, but it exceeds 2:1 at Alert, especially in early spring. Summer sulfate (and OM) at Alert, after June, is primarily biological with some transient contributions from biomass burning (BB). Utqiaġvik is likely similar, but has a larger contribution to OM from BB during the summer, giving the smaller SO4/OM value. In spring (and winter), both sites

experience transport from Eurasia with Utqiaġvik seeing a little more from Southeast Asia (e.g., Xu et al. 2017). OM relative to sulfate is similar at both sites.

The higher organic and non–sea salt sulfate mass concentration in summer in Antarctica is coincident with higher concentrations of CCN at supersaturations of 0.1% and 1% (Fig. 8a). This correlation means that the biogenic non–sea salt sulfate and organic sources may well both contribute significantly to summertime CCN concentrations, as they do in the Arctic (Abbatt et al. 2019). The relationship between biogenic non–sea salt sulfate and organic means that both can have an effect on cloud droplet number concentrations, potentially increasing cloud drop effective radius and shortwave reflection.

Examples of representative individual cases. Following these climatological comparisons, we now discuss some representative individual cases that illustrate the potential for evaluating climate model simulations with nearly identical multisensor datasets from both the Antarctic and the Arctic. AWARE obtained the first ever triple-wavelength radar observations of ice and mixed-phase clouds over Antarctica. These observations point to a new paradigm in unraveling ice microphysics processes at high latitudes. When observing ice particles with a single-wavelength radar in the "Rayleigh regime" (i.e., when the wavelength is large compared to the size of the ice particles), the radar reflectivity Z is proportional to the square of the particle masses $m(D)$ integrated over the particle size distribution (PSD) but it is more intricately related to other moments of the PSD, for example the cloud ice water content (IWC) or the ice mass flux, which are indeed the most relevant for microphysical studies. When the wavelength of the radars becomes comparable to the size of the particles being probed ("non-Rayleigh" regime) the measured reflectivity decreases sometimes by more than 10 dB relative to the Rayleigh reference (Matrosov 1998; Kneifel et al. 2011, 2015). The main reason for this decrease is that interferences (usually destructive) of the incident wave and reflected waves from different parts of the particle cause the backscattered energy to be smaller than for pure Rayleigh scatterers.

Dual-wavelength reflectivity ratios (DWR) are then indicative of a characteristic size of the PSD such as mass median diameter (Matrosov 1998; Kneifel et al. 2011). Depending on the radar wavelength pair,
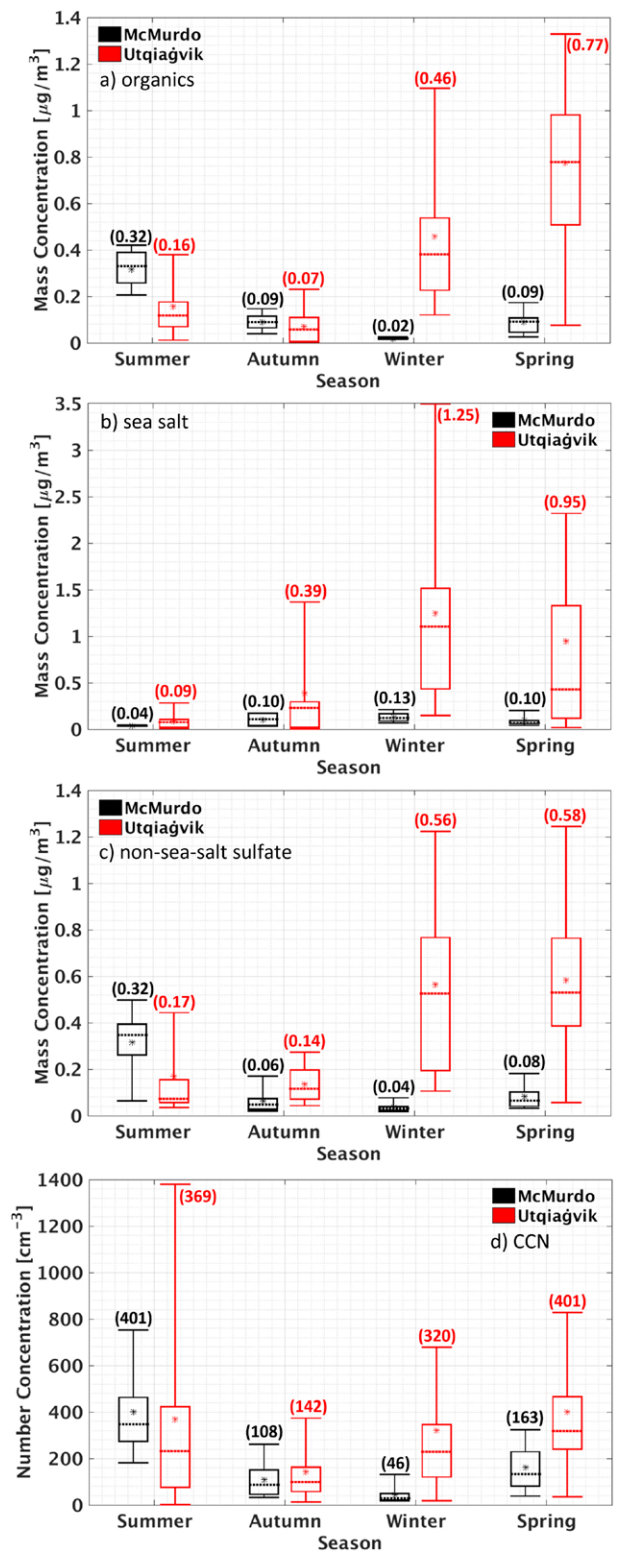

Fig. 10. Box-and-whisker diagrams of submicron mass concentrations for (a) organic, (b) sea salt, and (c) non–sea salt sulfate, and (d) CCN concentrations at 0.1% and 1%, designating the median (thick dotted line), 1st and 3rd quartiles (box edges), 5th and 95th percentiles (whiskers), and mean (asterisks). The McMurdo measurements are for 2016. The Utqiaġvik mass and CCN concentrations are for 2009. The Utqiaġvik CCN concentrations for 2009 were missing some supporting CN measurements so quality control was limited.

they are particularly effective within specific particle size ranges. For example, the Ka–W frequency pair is effective for a particle size range between 0.5 and 3 mm, whereas to cause a difference at X–Ka frequencies the particle size has to exceed sizes of ~8 mm. When more than two frequencies are considered not only can the characteristic size of the ice PSD be derived for broader size ranges but also information on bulk density can be gleaned (Kulie et al. 2014; Leinonen and Moisseev 2015; Kneifel et al. 2015; Stein et al. 2015), which better constrains the ice microphysics.

Figure 11 shows a two-dimensional histogram of the data collected at McMurdo during 10 January 2016 from the X–Ka- and W-band ARM radars. While most of the data are concentrated around the origin (0 dB, 0 dB), thereby corresponding to small ice crystals that produce the same reflectivities at all frequencies, histogram bins with large DWRs signal the presence of larger ice crystals. Following the rationale proposed by Kneifel et al. (2015) the three different branches indicated by the continuous, dotted and dashed lines correspond to different growth mechanisms. For example, the typical hook signature (continuous line) is likely associated with low-density aggregates, while the points with large Ka–W and small X–Ka DWR (dashed line) are linked to denser and more spherical particles. Retrieval methodologies focused at using this information in a quantitative way are currently under study (Leinonen et al. 2018; Chase et al. 2018; Mason et al. 2018; Tridon et al. 2019; Battaglia et al. 2020). Surprisingly, the strength of the observed multifrequency radar signatures are overall in a similar range (both DWRs exceeding 10 dB) as observed during the deployment of the AMF2 at the Biogenic Aerosols–Effects on Clouds and Climate (BAECC; Petäjä et al. 2016) campaign in Finland (Kneifel et al. 2015). The unexpected strong multifrequency radar signatures revealed during AWARE indicate that growth processes such as aggregation and riming play an important role in the processes related to snowfall production in Antarctica—at least in areas with sufficient supply of moisture such as close to the coast.

ARM's extensive multispectral capabilities deployed at McMurdo Station offer the ability to construct specific case studies for model evaluation (e.g., Silber et al. 2019b), as has been done with several Arctic field campaigns (e.g., Fridlind et al. 2007; Verlinde et al. 2007; McFarqhuar et al. 2011; Fridlind and Ackerman 2018). Here we demonstrate some AWARE ground-based remote sensing retrievals and contrasting Arctic cases from NSA. Figure 12
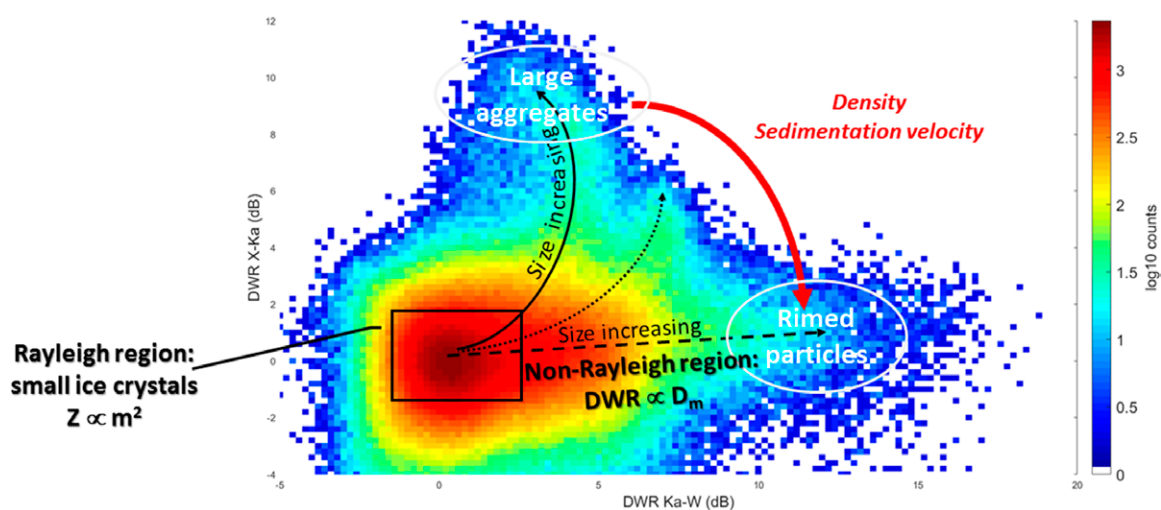

Fig. 11. Two-dimensional histogram of DWR Ka–W vs DWR X–Ka measurements collected by the X–Ka and W-band ARM radars during 10 Jan 2016 at McMurdo Station. Negative DWRs are unexpected and might be caused by imperfect radar volume matching and measurement noise. Away from the Rayleigh region (black square) different growth regimes can be identified (continuous, dotted, and dashed lines). The red arrow points toward ice particles characterized by higher densities and larger sedimentation velocities.

shows two representative examples of mixed-phase clouds observed at McMurdo and at the ARM NSA Utqiaġvik site as detected by the HSRL at visible wavelengths (532 nm) and the KAZR at millimeter wavelengths (~8.5 mm). As the two instruments operate at wavelengths that differ by four orders of magnitude, their measurements are sensitive to different aspects of the cloud. The lidar is more sensitive than radar to small particles with high number concentrations such as liquid droplets, as seen at the top of the cloud by a region of strong backscatter (Figs. 12a,b) and a low depolarization ratio indicating spherical droplets (Figs. 12c,d). Ice particles form in the layer of supercooled liquid water that precipitate from its base. This is seen as significantly nonzero lidar depolarization ratios indicating nonspherical particles (Figs. 12c,d) that are large enough to strongly reflect energy at the significantly longer radar wavelengths (Figs. 12e,f). The mixed-phase clouds shown are representative in that the clouds at Utqiaġvik tend to form in the boundary layer with the ice virga often reaching the surface,
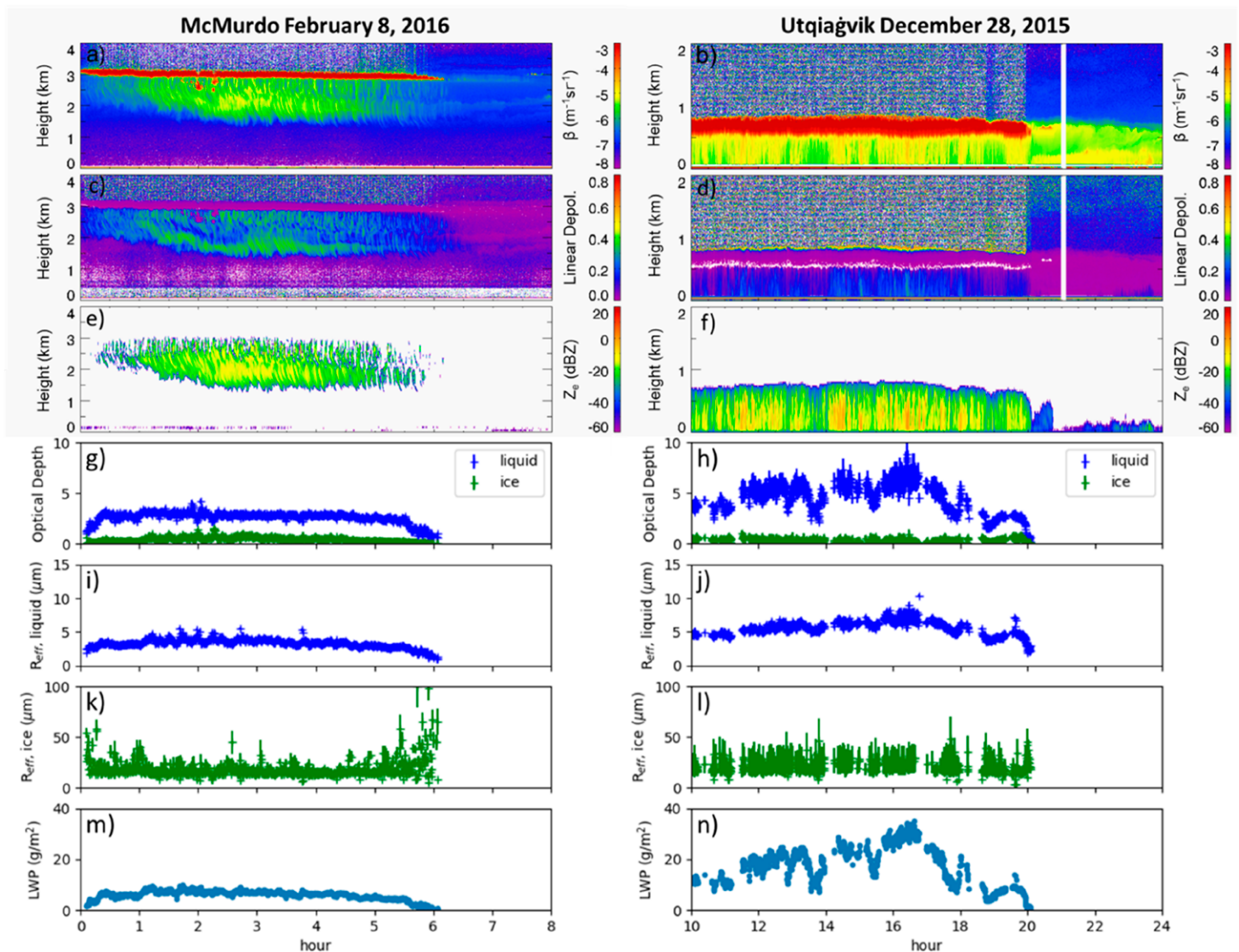

Fig. 12. Multispectral characterization of mixed-phase clouds at McMurdo during AWARE (8 Feb 2016) and at Utqiaġvik, Alaska (28 Dec 2015). Shown are time–height cross sections from zenith-pointing instruments: (a),(b) HSRL backscatter cross section β; (c),(d) HSRL linear depolarization ratio; and (e),(f) Ka-band radar reflectivity Z_e. Values for (a)–(f) are given by the color bars to the right of the panels. (g)–(m) Retrievals of (g),(h) optical depth (separately for ice and liquid phase); (i),(j) liquid water effective radius; (k),(l) ice particle effective radius; and (m),(n) LWP. The retrievals use downwelling infrared spectral radiances measured by the AERI via the method of Rowe et al. (2019, and references within). Retrieval uncertainty is indicated by the vertical extent of the symbols, obtained from the square root of the diagonal of the error covariance matrix for the state variable plotted.

while the McMurdo clouds tend to form above the boundary layer; the latter probably being related to the strong katabatic flow and other topographic effects (see Fig. 7; see also Silber et al. 2018a; Zhang et al. 2019).

Retrievals from the Atmospheric Emitted Radiance Interferometer (AERI) provide an important complement to the HSRL and radar measurements. The magnitude and spectral shape of the downwelling longwave radiance measured by the AERI from 8 to 25 μm is sensitive to cloud temperature, optical depth, thermodynamic phase, and particle effective radius. Cloud properties retrieved from AERI measurements using the Cloud and Atmospheric Radiation Retrieval Algorithm (CLARRA; Rowe et al. 2019) are shown in Figs. 11g–n.

The full year of measurements at McMurdo allows comparison of Arctic and Antarctic clouds over a full seasonal cycle. As an example, Fig. 12 compares Arctic and Antarctic clouds for two time periods. The dates were chosen such that temperatures are similar at the cloud heights (−30° to −20°C) and where supercooled cloud liquid water can exist. Although surface temperatures differed markedly for these two cases, four other cases were also considered for which surface temperatures were similar between locations (8 and 13 March 2016 at McMurdo, and 5 November 2014 and 20 January 2016 at Utqiaġvik; not shown). For all cases, the optical depth of liquid is higher than for ice (Figs. 12g,h) and variations in optical depth, liquid effective radius, and liquid water path are typically correlated with each other. However, differences are apparent in clouds between the two locations. At McMurdo clouds are higher (Figs. 12a–f) and optically thinner overall (Figs. 12g,h), and liquid droplets typically have smaller effective radii (Figs. 12i,j) for these cases. Similar contrasts were also found between the two locations for the other case examined. For example, the liquid effective radii at Utqiaġvik was found to be typically between 4 and 10 μm, in keeping with previous measurements in the Arctic (e.g., Cox et al. 2014), whereas at McMurdo it was typically below 5 μm. The latter is consistent with Zhang et al. (2019), who find similar small values for McMurdo using active-sensor techniques described in Snider et al. (2017). Work is in progress to retrieve and compare cloud microphysical properties including liquid and ice optical depths and effective particle sizes over a full year.

Climate modeling applications

The AWARE campaign's first major result came from WAIS Divide, when the sea container equipment recorded atmospheric and SEB fluxes at the edge of a major West Antarctic melt event (Nicolas et al. 2017). This melt event was associated with a strong El Niño year. The onset of the melt event on 10 January was accompanied by an abrupt temperature increase at WAIS Divide (Fig. 13). The immediate cause of this melt event was an amplified high pressure ridge ("blocking high") over the 90°–120°W sector of the Southern Ocean. By creating a prominent dent in the circumpolar westerly flow, this ridge generated a strong north–south advection of warm marine air toward West Antarctica. The ridge was strongest during 10–13 January 2016 but persisted through 20 January, maintaining warm conditions favorable to surface melt in the sector West Antarctica adjacent to the RIS. Positive sea surface temperature anomalies of >2°C near 50°S, 120°W provided additional heat to the air traveling south. The unusual extent and duration make the melt event one of the greatest observed in the RIS since the beginning of the satellite record in 1978 (Nicolas et al. 2017). The SEB evolution was derived from nearly all the AWARE instruments at WAIS Divide and is described in Nicolas et al. (2017). The "step function" in temperature and moisture throughout the lower troposphere that occurred around 10 January, captured by AWARE instruments, provides a unique case study for both regional and global climate models.

In Fig. 13 we show an evaluation of the Polar Weather Research and Forecasting regional model (PWRF), which is a version of the Weather Research and Forecasting (WRF) Model (Skamarock et al. 2008) adapted for high latitudes (e.g., Hines and Bromwich 2017); this comparison complements the comprehensive investigation by Hines et al. (2019) of the WAIS

Divide warming using PWRF simulations. Here PWRF uses a double-moment cloud microphysics scheme (Morrison et al. 2005), and is initialized in the first simulation using ERA-Interim (PWRF-EI; Dee et al. 2011) and then in the second using analysis data from the NOAA Global Forecast System (GFS; PWRF-FNL). Figure 12 focuses on the transition period 8–13 January 2016 when the step function in tropospheric temperature and moisture occurred. We first consider the precipitable water vapor (PWV), comparing both simulations against observations from the AWARE MWR retrievals. These WAIS Divide radiosonde data, used to derive the MWR PWV retrievals, were not contributed to the Global Telecommunication System (GTS) that feeds information into data assimilation for global meteorological reanalyses; and therefore we have an independent assessment of model performance at a completely data-sparse location. Both simulations capture much of the observed time evolution of this field, but there are key differences late on 10 January and throughout 11–12 January.

The PWV from the analysis/reanalysis should have a strong impact on the produced cloud liquid water in mesoscale simulations, and this is seen in the time evolution of cloud liquid water path (LWP). Observations show relatively high occurrence of liquid water on 9–10 January, and the simulations failed to capture this. The analyzed water vapor field may contribute to the error. The ERA-Interim simulation does a better job of capturing the liquid water early on the 11 January. Later in the day, more liquid water is simulated than observed. Liquid water is generally undersimulated on 12 January.

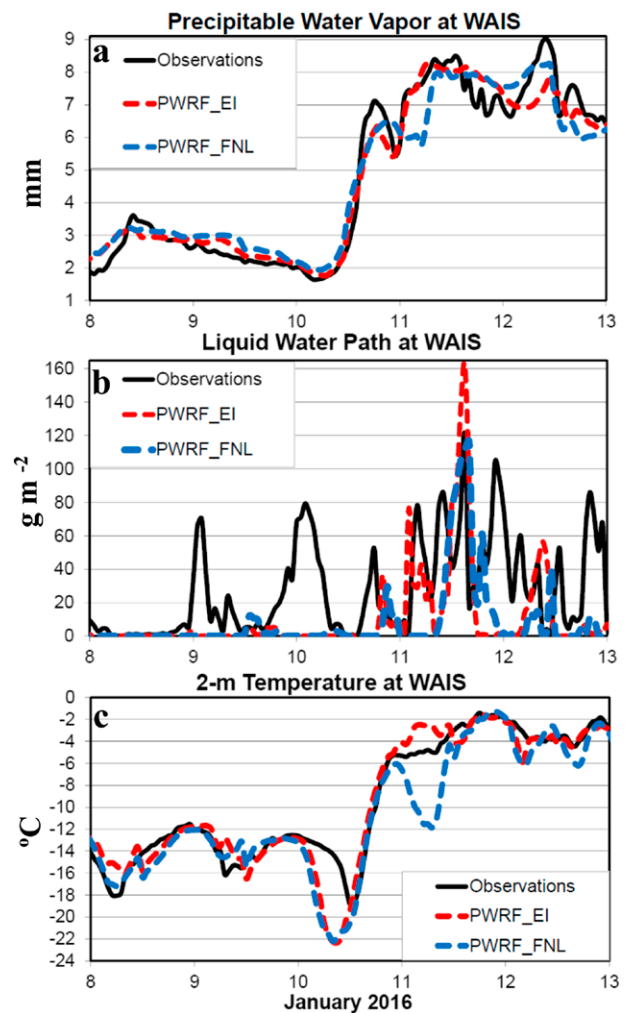Figure 13c shows the 2-m air temperature. The

Fig. 13. Simulation of the WAIS Divide melt event using PWRF, using input from ERA-Interim (PWRF-EI) and GFS (PWRF-FNL), compared against AWARE observations from radiosondes and microwave radiometer measurements: (top) near-surface (2-m) air temperature, (middle) cloud LWP, and (bottom) vertically integrated PWV.

near-surface temperature should be important for tracking West Antarctic melting. Early on 10 January, little cloud liquid water is simulated, and as a possible result the simulations are several degrees too cold. However, much of the warming event during the latter half of 10 January is captured by the simulations (cf. Figs. 13a and 13c). The simulation driven by ERA-Interim better captures the liquid water during the first half of the 11 January, so it better represents the temperature.

Figure 14 illustrates a global climate model (GCM) evaluation example, for GCMs presently under development, again using the WAIS Divide melt event data as a case study. The models considered here are the first version of the atmospheric component of the DOE Energy Exascale Earth System Model (E3SM), EAMv1 (see Rasch et al. 2019), and the most recent update of the NASA Goddard Institute for Space Studies (GISS) GCM (Schmidt et al. 2014), the ModelE. Fields used to nudge horizontal winds in ModlE3 and run EAMv1 are taken from ERA5, the fifth-generation atmospheric reanalysis from the European Centre for Medium-Range Weather Forecasts (ECMWF; Hersbach and Dee 2016). Results show that both models generally simulate the PWV well (Fig. 14a), but that both models overestimate the LWP of the supercooled clouds, particularly for E3SMv1 (Fig. 14b). These overestimations have important

consequences to the amount of energy into the snowpack (netSnowpack) at the WAIS Divide, computed as the residual of the net shortwave and longwave radiative energy (netRadiation) into the surface minus the turbulent fluxes (sensible and latent heating) removing energy from the surface (netTurbulence):

$$netSnowpack = netRadiation - netTurbulence. \qquad (1)$$

An interesting interplay is seen among these terms in Figs. 14c–e. The netRadiation term for both models tends to have a positive bias (too much energy into the snowpack), although ModelE has a greater day-to-day oscillation about zero net flux than does EAMv1 (Fig. 14c). The turbulent flux of energy away from the snowpack's surface, netTurbulence, is positively biased for EAMv1 while ModelE generally performs well (Fig. 14d). The net effect of the radiative and turbulent fluxes on the energy into the snowpack (Fig. 14e) shows that the positive biases for EAMv1 largely cancel, while the oscillatory nature of the radiative component for ModelE tends to dominate its good simulation of the surface turbulence. A likely contributor to the radiative biases for both models is the change in the surface longwave radiative flux resulting from errors in the LWP that affect cloud emissivity (e.g., Silber et al. 2019c). Figure 14f shows the model bias relative to observations of the net longwave radiation at the surface versus the LWP bias. The plot shows a clear tendency for overestimates in LWP to yield overestimates in surface longwave flux, and vice versa, indicating that the LWP bias is an important factor. Collectively, the results in this figure demonstrate the ability to attribute model biases using component analyses made available from the AWARE data.

Fig. 14. GCM evaluations at the WAIS Divide during the 2016 West Antarctic melt event for the DOE EAMv1 and GISS ModelE. EAMv1 simulations are run in hindcast mode (Ma et al. 2015) initialized using ERA5 with the 12–36-h hindcast period shown here. The GISS ModelE simulation is nudged to ERA5. The EAMv1 (red) and ModelE (blue) simulations are compared with observations (black) of (a) PWV and (b) cloud LWP, both retrieved from surface microwave radiometer data. The primary warming period is indicated by gray shading. Model–observation differences for net surface fluxes are shown for (c) total net radiation (longwave plus shortwave), (d) total turbulence (sensible and latent heat, with the sign being positive toward the atmosphere), and (e) total energy into the snowpack. (f) Scatterplot of the model–observation differences in net longwave flux at the surface (LW) vs differences in LWP. The observational data in (a)–(f) are described in Nicolas et al. (2017).
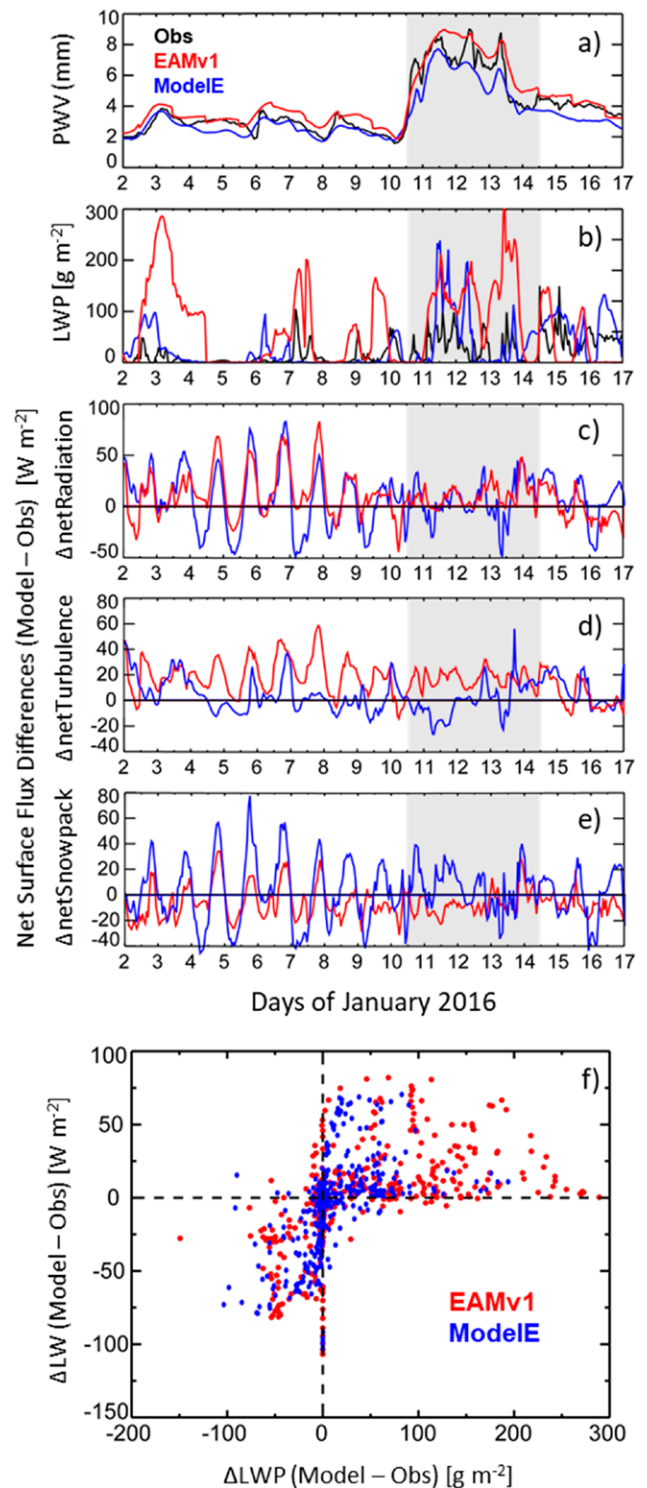
Summary and future work

Any time-limited field campaign, even one such as AWARE with its robust suite of instruments and relatively longer duration (1 year), has associated issues regarding representativeness. Geographically, the AMF2 deployment at McMurdo sampled an Antarctic coastal location with adjacent high terrain with complex topography, such that cloud formation and persistence are often influenced by katabatic flows and/or terrain-induced gravity waves. This general situation might apply to numerous coastal Antarctic locations. The AWARE instrumentation at WAIS Divide sampled the SEB under cloud cover representative of most of West Antarctica (e.g., Scott et al. 2017), although WAIS Divide is at a much higher elevation than the West Antarctic ice shelves that are most vulnerable to a warming climate. Hence, the SEB measurements during the January 2016 melt event describe a precursor to and onset of surface melt, rather than a fully developed surface melt that directly impacts an ice shelf or ice cliff via hydrofracturing. AWARE did not make any measurements on the high terrain of East Antarctica, and so a researcher should be very careful about generalizing AWARE findings in cloud physics or aerosol microphysics and chemistry to East Antarctica. Regarding climatology of the specific regions sampled, AWARE trailed a large ENSO event and was then followed by unprecedented sea ice loss and another extensive surface melt event the following spring linked to strong negative southern annular mode (SAM) index combined with a positive index in the first Pacific–South America pattern having a classic Rossby wave train structure (Scott et al. 2019). AWARE data from both McMurdo Station and WAIS Divide might therefore be representative of warmer than normal conditions compared with recent climatology.

Although separated by 1,600 km, there is often a meteorological relationship between the two AWARE sites at McMurdo Station and WAIS Divide Ice Camp. Low pressure troughs in the Ross Sea frequently bring moisture and cloud cover over the WAIS, which can eventually descend onto the Ross Ice Shelf and reach Ross Island from a southerly direction (Coggins et al. 2014; Nigro and Cassano 2014; Silber et al. 2019a). This is particularly evident in case studies described in Scott and Lubin (2014). In contrast to the Arctic, this airmass trajectory also traverses mountain ranges that cause substantial orographic lifting and related ice cloud formation (Scott and Lubin 2016). Tracking of these synoptic-scale patterns by satellite remote sensing and validation of the "end point" in cloud evolution from AWARE measurements at McMurdo might provide further insight into mixed-phase cloud properties that are distinct from the Arctic.

In the first Antarctic climatological assessment from AWARE data presented here, we have seen many contrasts with the high Arctic. These include persistent differences in liquid cloud occurrence, cloud height, and cloud thickness. Antarctic aerosol properties are also quite different from the Arctic, due to the continent's isolation from lower latitudes by Southern Ocean storm tracks. This brings a seasonal cycle in which most aerosol constituents have maximum concentration in summer, and in which abundances are almost entirely from a variety of Antarctic rather than transported sources. Comparable measurements from two high Arctic sites show springtime maxima comprising the "Arctic haze" that has origins from northern midlatitudes. AWARE data show that Antarctic aerosol abundances are not negligible despite the large-scale dynamical isolation, and the aerosol chemical composition revealed by AWARE measurements implies that aerosol–cloud interaction in the Antarctic deserves further study.

In the preliminary model evaluations presented here, we have considered the WAIS Divide case study sufficiently to note some basic discrepancies between simulations and observations. Much work needs to be done on the specific cloud microphysical parameterizations, or other model components, to realize improvements to model performance over Antarctica. The AMF2 data are an additional resource for developing very stringent tests of mixed-phase cloud parameterization performance. In addition to the orographic forcing by the Transantarctic Mountains that causes climatological contrasts from the Arctic, terrain variability in the local

Ross Island area often induces low-level gravity waves that produce unique mixed-phase cloud realizations. The AWARE science team is presently constructing some AMF2 case studies that might be suitable for model evaluation and improvement, and many coauthors on this paper already have experience with AWARE data that could assist other researchers with selecting data for a variety of modeling requirements. Finally, AWARE data should be valuable for planning future Antarctic fieldwork using advanced instrumentation. Examination of the AWARE campaign data in the online ARM Archive can provide guidance for what to expect when various types of meteorological and remote sensing equipment are deployed for extended Antarctic research programs.

References

Abbatt, J. P. D., and Coauthors, 2019: Overview paper: New insights into aerosol and climate in the Arctic. *Atmos. Chem. Phys.*, **19**, 2527–2560, https://doi.org/10.5194/acp-19-2527-2019.

Alley, R. B., S. Anandakrishnan, K. Christianson, H. J. Horgan, A. Muto, B. R. Parizek, D. Pollard, and R. T. Walker, 2015: Oceanic forcing of ice-sheet retreat: West Antarctica and more. *Annu. Rev. Earth Planet. Sci.*, **43**, 207–231, https://doi.org/10.1146/annurev-earth-060614-105344.

Barrie, L. A., and R. M. Hoff, 1985: Five years of air chemistry observations in the Canadian Arctic. *Atmos. Environ.*, **19**, 1995–2010, https://doi.org/10.1016/0004-6981(85)90108-8.

Bassis, J. N., and S. Jacobs, 2013: Diverse calving patterns linked to glacier geometry. *Nat. Geosci.*, **6**, 833–836, https://doi.org/10.1038/ngeo1887.

Bates, T. S., and Coauthors, 2012: Measurements of ocean derived aerosol off the coast of California. *J. Geophys. Res.*, **117**, D00V15, https://doi.org/10.1029/2012JD017588.

Battaglia, A., S. Tanelli, F. Tridon, S. Kneifel, J. Leinonen, and P. Kollias, 2020: Triple-frequency radar retrievals. *Satellite Precipitation Measurement*, V. Levizzani et al., Ed., Springer, 211–229.

Bennartz, R., and Coauthors, 2013: July 2012 Greenland melt extent enhanced by low-level liquid clouds. *Nature*, **496**, 83–86, https://doi.org/10.1038/nature12002.

Bromwich, D. H., and Coauthors, 2012: Tropospheric clouds in Antarctica. *Rev. Geophys.*, **50**, RG1004, https://doi.org/10.1029/2011RG000363.

——, J. P. Nicolas, A. J. Monaghan, M. A. Lazzara, L. M. Keller, G. A. Weidner, and A. B. Wilson, 2013: Central West Antarctica among the most rapidly warming regions on Earth. *Nat. Geosci.*, **6**, 139–145, https://doi.org/10.1038/ngeo1671.

Chase, R. J., and Coauthors, 2018: Evaluation of triple-frequency radar retrieval of snowfall properties using coincident airborne in situ observations during OLYMPEX. *Geophys. Res. Lett.*, **45**, 5752–5760, https://doi.org/10.1029/2018GL077997.

Clothiaux, E. E., and Coauthors, 2001: The ARM Millimeter Wave Cloud Radars (MMCRs) and the Active Remote Sensing of Clouds (ARSCL) Value Added Product (VAP). DOE Tech. Memo. ARM VAP002.1, 55 pp., https://www.arm.gov/publications/tech_reports/arm-vap-002-1.pdf.

Coggins, J. A., A. J. McDonald, and B. Jolly, 2014: Synoptic climatology of the Ross Ice Shelf and Ross Sea region of Antarctica: K-means clustering and validation. *Int. J. Climatol.*, **34**, 2330–2348, https://doi.org/10.1002/joc.3842.

Cox, C. J., D. D. Turner, P. M. Rowe, and M. D. Shupe, 2014: Cloud microphysical properties retrieved from downwelling infrared radiance measurements made at Eureka, Nunavut, Canada (2006–09). *J. Appl. Meteor. Climatol.*, **53**, 772–791, https://doi.org/10.1175/JAMC-D-13-0113.1.

DeConto, R. M., and D. Pollard, 2016: Contributions of Antarctica to past and future sea-level rise. *Nature*, **531**, 591–597, https://doi.org/10.1038/nature17145.

Dee, D. P., and Coauthors, 2011: The ERA-Interim reanalysis: Configuration and performance of the data assimilation system. *Quart. J. Roy. Meteor. Soc.*, **137**, 553–597, https://doi.org/10.1002/qj.828.

Ding, Q., E. J. Steig, D. S. Battisti, and M. Küttel, 2011: Winter warming in West Antarctica caused by central tropical Pacific warming. *Nat. Geosci.*, **4**, 398–403, https://doi.org/10.1038/ngeo1129.

Elvidge, A. D., I. A. Renfrew, J. C. King, A. Orr, T. A. Lachlan-Cope, M. Weeks, and S. L. Gray, 2015: Foehn jets over the Larsen C Ice Shelf, Antarctica. *Quart. J. Roy. Meteor. Soc.*, **141**, 698–713, https://doi.org/10.1002/qj.2382.

Fridlind, A. M., and A. S. Ackerman, 2018: Simulations of Arctic mixed-phase boundary layer clouds: Advances in understanding and outstanding questions. *Mixed-Phase Clouds*, C. Andronache, Ed., Elsevier, 153–183, https://doi.org/10.1016/B978-0-12-810549-8.00007-6.

——, ——, G. McFarquhar, G. Zhang, M. R. Poellot, P. J. DeMott, A. J. Prenni, and A. J. Heymsfield, 2007: Ice properties of single-layer stratocumulus during the Mixed-Phase Arctic Cloud experiment: 2. Model results. *J. Geophys. Res.*, **112**, D24202, https://doi.org/10.1029/2007JD008646.

Frossard, A. A., P. M. Shaw, L. M. Russell, J. H. Kroll, M. R. Canagaratna, D. R. Worsnop, P. K. Quinn, and T. S. Bates, 2011: Springtime Arctic haze contributions of submicron organic particles from European and Asian combustion sources. *J. Geophys. Res.*, **116**, D05205, https://doi.org/10.1029/2010JD015178.

Fürst, J. J., H. Goelzer, and P. Huybrechts, 2015: Ice-dynamic projections of the Greenland ice sheet in response to atmospheric and oceanic warming. *Cryosphere*, **9**, 1039–1062, https://doi.org/10.5194/tc-9-1039-2015.

——, G. Durand, F. Gillet-Chaulet, L. Tavard, M. Rankl, M. Braun, and O. Gagliardini, 2016: The safety band of Antarctic ice shelves. *Nat. Climate Change*, **6**, 479–482, https://doi.org/10.1038/nclimate2912.

Gorodetskaya, I. V., and Coauthors, 2015: Cloud and precipitation properties from ground-based remote-sensing instruments in East Antarctica. *Cryosphere*, **9**, 285–304, https://doi.org/10.5194/tc-9-285-2015.

Grazioli, J., J.-B. Madeleine, H. Gallée, R. M. Forbes, C. Genthon, G. Krinner, and A. Berne, 2017: Katabatic winds diminish precipitation contribution to the Antarctic ice mass balance. *Proc. Natl. Acad. Sci. USA*, **114**, 10858–10863, https://doi.org/10.1073/pnas.1707633114.

Hersbach, H., and D. Dee, 2016: ERA5 reanalysis is in production. *ECMWF Newsletter, No. 147, ECMWF, Reading, United Kingdom, 7*, https://www.ecmwf.int/sites/default/files/elibrary/2016/16299-newsletter-no147-spring-2016.pdf.

Hines, K. M., and D. H. Bromwich, 2017: Simulation of late summer Arctic clouds during ASCOS with Polar WRF. *Mon. Wea. Rev.*, **145**, 521–541, https://doi.org/10.1175/MWR-D-16-0079.1.

——, ——, S.-H. Wang, I. Silber, J. Verlinde, and D. Lubin, 2019: Microphysics of summer clouds in central West Antarctica simulated by Polar WRF and the Antarctic Mesoscale Prediction System (AMPS). *Atmos. Chem. Phys.*, **19**, 12431–12454, https://doi.org/10.5194/acp-19-12431-2019.

Hu, X., S. A. Sejas, M. Cai, Z. Li, and S. Yang, 2019: Atmospheric dynamics footprint on the January 2016 ice sheet melting in West Antarctica. *Geophys. Res. Lett.*, **46**, 2829–2835, https://doi.org/10.1029/2018GL081374.

Hyder, P., and Coauthors, 2018: Critical Southern Ocean climate model biases traced to atmospheric model cloud errors. *Nat. Commun.*, **9**, 3625, https://doi.org/10.1038/s41467-018-05634-2.

Jolly, B., P. Kuma, A. McDonald, and S. Parsons, 2018: An analysis of the cloud environment over the Ross Sea and Ross Ice Shelf using CloudSat/CALIPSO satellite observations: The importance of synoptic forcing. *Atmos. Chem. Phys.*, **18**, 9723–9739, https://doi.org/10.5194/acp-18-9723-2018.

Joughin, I., B. E. Smith, and B. Medley, 2014: Marine ice sheet collapse potentially under way for the Thwaites Glacier Basin, West Antarctica. *Science*, **344**, 735–738, https://doi.org/10.1126/science.1249055.

Kingslake, J., J. C. Ely, I. Das, and R. E. Bell, 2017: Widespread movement of meltwater onto and across Antarctic ice shelves. *Nature*, **544**, 349–352, https://doi.org/10.1038/nature22049.

Kneifel, S., M. S. Kulie, and R. Bennartz, 2011: A triple-frequency approach to retrieve microphysical snowfall parameters. *J. Geophys. Res.*, **116**, D11203, https://doi.org/10.1029/2010JD015430.

——, A. von Lerber, J. Tiira, D. Moisseev, P. Kollias, and J. Leinonen, 2015: Observed relations between snowfall microphysics and triple-frequency radar measurements. *J. Geophys. Res. Atmos.*, **120**, 6034–6055, https://doi.org/10.1002/2015JD023156.

Kulie, M. S., M. J. Hiley, R. Bennartz, S. Kneifel, and S. Tanelli, 2014: Triple-frequency radar reflectivity signatures of snow: Observations and comparisons with theoretical ice particle scattering models. *J. Appl. Meteor. Climatol.*, **53**, 1080–1098, https://doi.org/10.1175/JAMC-D-13-066.1.

Lachlan-Cope, T., C. Listowski, and S. O'Shea, 2016: The microphysics of clouds over the Antarctic Peninsula – Part 1: Observations. *Atmos. Chem. Phys.*, **16**, 15605–15617, https://doi.org/10.5194/acp-16-15605-2016.

Law, K. S., and A. Stohl, 2007: Arctic air pollution: Origins and impacts. *Science*, **315**, 1537–1540, https://doi.org/10.1126/science.1137695.

Lawson, R. P., and A. Gettelman, 2014: Impact of Antarctic mixed-phase clouds on climate. *Proc. Natl. Acad. Sci. USA*, **111**, 18156–18161, https://doi.org/10.1073/pnas.1418197111.

Lazzara, M. A., G. A. Weidner, L. M. Keller, J. E. Thom, and J. J. Cassano, 2012: Antarctic automatic weather station program: 30 years of polar observations. *Bull. Amer. Meteor. Soc.*, **93**, 1519–1537, https://doi.org/10.1175/BAMS-D-11-00015.1.

Leaitch, W. R., and Coauthors, 2018: Organic functional groups in the submicron aerosol at 82.5°N, 62.5°W from 2012 to 2014. *Atmos. Chem. Phys.*, **18**, 3269–3287, https://doi.org/10.5194/acp-18-3269-2018.

Legrand, M., F. Ducroz, D. Wagenbach, R. Mulvaney, and J. Hall, 1998: Ammonium in coastal Antarctic aerosol and snow: Role of polar ocean and penguin emissions. *J. Geophys. Res.*, **103**, 11 043–11 056, https://doi.org/10.1029/97JD01976.

——, V. Gros, S. Preunkert, R. Sarda-Esteve, A. M. Thierry, G. Pepy, and B. Jourdain, 2012: A reassessment of the budget of formic and acetic acids in the boundary layer at Dumont d'Urville (coastal Antarctica): The role of penguin emissions on the budget of several oxygenated volatile organic compounds. *J. Geophys. Res.*, **117**, D06308, https://doi.org/10.1029/2011JD017102.

Leinonen, J., and D. Moisseev, 2015: What do triple-frequency radar signatures reveal about aggregate snowflakes? *J. Geophys. Res. Atmos.*, **120**, 229–239, https://doi.org/10.1002/2014JD022072.

——, and Coauthors, 2018: Retrieval of snowflake microphysical properties from multi-frequency radar observations. *Atmos. Meas. Tech.*, **11**, 5471–5488, https://doi.org/10.5194/amt-11-5471-2018.

Liu, J., and Coauthors, 2018: High summertime aerosol organic functional group concentrations from marine and seabird sources at Ross Island, Antarctica, during AWARE. *Atmos. Chem. Phys.*, **18**, 8571–8587, https://doi.org/10.5194/acp-18-8571-2018.

Ma, H.-Y., and Coauthors, 2015: An improved hindcast approach for evaluation and diagnosis of physical processes in global climate models. *J. Adv. Model. Earth Syst.*, **7**, 1810–1827, https://doi.org/10.1002/2015MS000490.

Maahn, M., C. Burgard, S. Crewell, I. V. Gorodetskaya, S. Kneifel, S. Lhermite, K. Van Tricht, and N. P. M. van Lipzig, 2014: How does the spaceborne radar blind zone affect derived surface snowfall statistics in polar regions? *J. Geophys. Res. Atmos.*, **119**, 13 604–13 620, https://doi.org/10.1002/2014JD022079.

Mason, S. L., C. J. Chiu, R. J. Hogan, D. Moisseev, and S. Kneifel, 2018: Retrievals of riming and snow density from vertically pointing Doppler radars. *J. Geophys. Res. Atmos.*, **123**, 13 807–13 834, https://doi.org/10.1029/2018JD028603.

Mather, J. H., and J. W. Voyles, 2013: The ARM Climate Research Facility: A review of structure and capabilities. *Bull. Amer. Meteor. Soc.*, **94**, 377–392, https://doi.org/10.1175/BAMS-D-11-00218.1.

Matrosov, S. Y., 1998: A dual-wavelength radar method to measure snowfall rate. *J. Appl. Meteor.*, **37**, 1510–1521, https://doi.org/10.1175/1520-0450(1998)037<1510:ADWRMT>2.0.CO;2.

McFarquhar, G. M., and Coauthors, 2011: Indirect and semi-direct aerosol campaign: The impact of Arctic aerosols on clouds. *Bull. Amer. Meteor. Soc.*, **92**, 183–201, https://doi.org/10.1175/2010BAMS2935.1.

Monaghan, A. J., D. H. Bromwich, J. G. Powers, and K. W. Manning, 2005: The climate of the McMurdo, Antarctica, region as represented by one year of forecasts from the Antarctic mesoscale prediction system. *J. Climate*, **18**, 1174–1189, https://doi.org/10.1175/JCLI3336.1.

Morrison, H., J. A. Curry, and V. I. Khvorostyanov, 2005: A new double-moment microphysics scheme for application in cloud and climate models. Part I: Description. *J. Atmos. Sci.*, **62**, 1665–1677, https://doi.org/10.1175/JAS3446.1.

——, G. de Boer, G. Feingold, J. Harrington, M. D. Shupe, and K. Sulia, 2012: Resilience of persistent Arctic mixed-phase clouds. *Nat. Geosci.*, **5**, 11–17, https://doi.org/10.1038/NGEO1332.

Nicolas, J. P., and D. H. Bromwich, 2011: Climate of West Antarctica and influence of marine air intrusions. *J. Climate*, **24**, 49–67, https://doi.org/10.1175/2010JCLI3522.1.

——, and ——, 2014: New reconstruction of Antarctic near-surface temperatures: Multidecadal trends and reliability of global reanalyses. *J. Climate*, **27**, 8070–8093, https://doi.org/10.1175/JCLI-D-13-00733.1.

——, and Coauthors, 2017: January 2016 extensive summer melt in West Antarctica favored by strong El Niño. *Nat. Commun.*, **8**, 15799, https://doi.org/10.1038/ncomms15799.

Nigro, M. A., and J. J. Cassano, 2014: Analysis of the Ross Ice Shelf airstream forcing mechanisms using self-organizing maps. *Mon. Wea. Rev.*, **142**, 4719–4734, https://doi.org/10.1175/MWR-D-14-00077.1.

Oppenheimer, M., 1998: Global warming and the stability of the West Antarctic Ice Sheet. *Nature*, **393**, 325–332, https://doi.org/10.1038/30661.

Paolo, F. S., H. A. Fricker, and L. Padman, 2015: Volume loss from Antarctic ice shelves is accelerating. *Science*, **348**, 327–331, https://doi.org/10.1126/science.aaa0940.

Peppler, R. A., and Coauthors, 2008: An overview of ARM Program Climate Research Facility data quality assurance. *Open Atmos. Sci. J.*, **2**, 192–216, https://doi.org/10.2174/1874282300802010192.

Peters, W., and Coauthors, 2007: An atmospheric perspective on North American carbon dioxide exchange: CarbonTracker. *Proc. Natl. Acad. Sci. USA*, **104**, 18 925–18 930, https://doi.org/10.1073/pnas.0708986104.

Petäjä, T., and Coauthors, 2016: BAECC: A field campaign to elucidate the impact of biogenic aerosols on clouds and climate. *Bull. Amer. Meteor. Soc.*, **97**, 1909–1928, https://doi.org/10.1175/BAMS-D-14-00199.1.

Pollard, D., R. M. DeConto, and R. B. Alley, 2015: Potential Antarctic ice sheet retreat driven by hydrofracturing and ice cliff failure. *Earth Planet. Sci. Lett.*, **412**, 112–121, https://doi.org/10.1016/j.epsl.2014.12.035.

Pritchard, H. D., S. R. M. Ligtenberg, H. A. Fricker, D. G. Vaughan, M. R. van den Broeke, and L. Padman, 2012: Antarctic ice-sheet loss driven by basal melting of ice shelves. *Nature*, **484**, 502–505, https://doi.org/10.1038/nature10968.

Quinn, P. K., T. L. Miller, T. S. Bates, J. A. Ogren, E. Andrews, and G. E. Shaw, 2002: A 3-year record of simultaneously measured aerosol chemical and optical properties at Barrow, Alaska. *J. Geophys. Res.*, **107**, 4130, https://doi.org/10.1029/2001JD001248.

——, G. E. Shaw, E. Andrews, E. G. Dutton, T. Ruoho-Airola, and S. L. Gong, 2007: Arctic haze: Current trends and knowledge gaps. *Tellus*, **59B**, 99–114, https://doi.org/10.1111/J.1600-0889.2006.00236.X.

Rasch, P. J., and Coauthors, 2019: An overview of the atmospheric component of the Energy Exascale Earth System Model. *J. Adv. Model. Earth Syst.*, **11**, 2377–2411, https://doi.org/10.1029/2019MS001629.

Ricaud, P., E. Bazile, M. del Guasta, C. Lanconelli, P. Grignioni, and A. Mahjoub, 2017: Genesis of diamond dust, ice fog and thick cloud episodes observed and modeled above Dome C, Antarctica. *Atmos. Chem. Phys.*, **17**, 5221–5237, https://doi.org/10.5194/acp-17-5221-2017.

Rignot, E., J. Mouginot, M. Morlighem, H. Seroussi, and B. Scheuchl, 2014: Widespread, rapid grounding line retreat of Pine Island, Thwaites, Smith, and Kohler glaciers, West Antarctica, from 1992-2011. *Geophys. Res. Lett.*, **41**, 3502–3509, https://doi.org/10.1002/2014GL060140.

Rowe, P. M., C. J. Cox, S. Neshyba, and V. P. Walden, 2019: Toward autonomous surface-based infrared remote sensing of polar clouds: Retrievals of cloud optical and microphysical properties. *Atmos. Meas. Tech.*, **12**, 5071–5086, https://doi.org/10.5194/amt-12-5071-2019.

Scott, R. C., D. Lubin, A. M. Vogelmann, and S. Kato, 2017: West Antarctic Ice Sheet cloud cover and surface radiation budget from NASA A-Train satellites. *J. Climate*, **30**, 6151–6170, https://doi.org/10.1175/JCLI-D-16-0644.1.

Scambos, T. A., C. Hulbe, M. Fahnestock, and J. Bohlander, 2000: The link between climate warming and break-up of ice shelves in the Antarctic Peninsula. *J. Glaciol.*, **46**, 516–530, https://doi.org/10.3189/172756500781833043.

Schmale, J., and Coauthors, 2013: Sub-Antarctic marine aerosol: Dominant contributions from biogenic sources. *Atmos. Chem. Phys.*, **13**, 8669–8694, https://doi.org/10.5194/acp-13-8669-2013.

Schmidt, G. A., and Coauthors, 2014: Configuration and assessment of the GISS ModelE2 contributions to the CMIP5 archive. *J. Adv. Model. Earth Syst.*, **6**, 141–184, https://doi.org/10.1002/2013MS000265.

Schneider, D. P., C. Deser, and Y. Okumura, 2012: An assessment and interpretation of the observed warming of West Antarctica in the austral spring. *Climate Dyn.*, **38**, 323–347, https://doi.org/10.1007/s00382-010-0985-x.

Scott, R. C., and D. Lubin, 2014: Mixed-phase cloud radiative properties over Ross Island: The influence of various synoptic-scale atmospheric circulation regimes. *J. Geophys. Res. Atmos.*, **119**, 6702–6723, https://doi.org/10.1002/2013JD021132.

——, and ——, 2016: Unique manifestations of mixed-phase cloud microphysics over Ross Island and the Ross Ice Shelf, Antarctica. *Geophys. Res. Lett.*, **43**, 2936–2945, https://doi.org/10.1002/2015GL067246.

——, J. P. Nicolas, D. H. Bromwich, J. R. Norris, and D. Lubin, 2019: Meteorological drivers and large-scale climate forcing of West Antarctic surface melt. *J. Climate*, **32**, 665–684, https://doi.org/10.1175/JCLI-D-18-0233.1.

Shaw, G. E., 1982: Evidence for a central Eurasian source area of Arctic haze in Alaska. *Nature*, **299**, 815–818, https://doi.org/10.1038/299815a0.

Shaw, P. M., L. M. Russell, A. Jefferson, and P. K. Quinn, 2010: Arctic organic aerosol measurements show particles from mixed combustion in spring haze and from frost flowers in winter. *Geophys. Res. Lett.*, **37**, L10803, https://doi.org/10.1029/2010GL042831.

Shupe, M. D., 2011: Clouds at Arctic atmospheric observatories. Part II: Thermodynamic phase characteristics. *J. Appl. Meteor. Climatol.*, **50**, 645–661, https://doi.org/10.1175/2010JAMC2468.1.

Silber, I., J. Verlinde, E. W. Eloranta, and M. Cadeddu, 2018a: Antarctic cloud macrophysical, thermodynamic phase, and atmospheric inversion coupling properties at McMurdo station: 1. Principal data processing and climatology. *J. Geophys. Res. Atmos.*, **123**, 6099–6121, https://doi.org/10.1029/2018JD028279.

——, ——, ——, C. J. Flynn, and D. M. Flynn, 2018b: Polar liquid cloud base detection algorithms for high spectral resolution or micropulse lidar data. *J. Geophys. Res. Atmos.*, **123**, 4310–4322, https://doi.org/10.1029/2017JD027840.

——, ——, M. Cadeddu, C. J. Flynn, A. M. Vogelmann, and E. W. Eloranta, 2019a: Antarctic cloud macrophysical, thermodynamic phase, and atmospheric inversion coupling properties at McMurdo Station. Part II: Radiative impact during different synoptic regimes. *J. Geophys. Res. Atmos.*, **124**, 1697–1719, https://doi.org/10.1029/2018JD029471.

——, and Coauthors, 2019b: Persistent supercooled drizzle at temperatures below −25°C observed at McMurdo Station, Antarctica. *J. Geophys. Res. Atmos.*, **124**, 10878–10895, https://doi.org/10.1029/2019JD030882.

——, J. Verlinde, S.-H. Wang, D. H. Bromwich, A. M. Fridlind, M. Cadeddu, and E. W. Eloranta, 2019c: Cloud influence on ERA5 and AMPS surface downwelling longwave radiation biases in West Antarctica. *J. Climate*, **32**, 7935–7949, https://doi.org/10.1175/JCLI-D-19-0149.1.

Skamarock, W. C., and Coauthors, 2008: A description of the Advanced Research WRF version 3. NCAR Tech. Note NCAR/TN-475+STR, 113 pp., https://doi.org/10.5065/D68S4MVH.

Snider, J. R., D. Leon, and Z. Wang, 2017: Droplet concentration and spectral broadening in Southeast Pacific stratocumulus clouds. *J. Atmos. Sci.*, **74**, 719–749, https://doi.org/10.1175/JAS-D-16-0043.1.

Stein, T. H. M., C. D. Westbrook, and J. C. Nicol, 2015: Fractal geometry of aggregate snowflakes revealed by triple-wavelength radar measurements. *Geophys. Res. Lett.*, **42**, 176–183, https://doi.org/10.1002/2014GL062170.

Town, M. S., V. P. Walden, and S. G. Warren, 2007: Cloud cover over the South Pole from visual observations, satellite retrievals, and surface-based infrared radiation measurements. *J. Climate*, **20**, 544–559, https://doi.org/10.1175/JCLI4005.1.

Trenberth, K. E., and J. T. Fasullo, 2010: Simulation of present day and twenty first century energy budgets of the Southern Oceans. *J. Climate*, **23**, 440–454, https://doi.org/10.1175/2009JCLI3152.1.

Tridon, F., and Coauthors, 2019: The microphysics of stratiform precipitation during OLYMPEX: Compatibility between triple-frequency radar and airborne in situ observations. *J. Geophys. Res. Atmos.*, **124**, 8764–8792, https://doi.org/10.1029/2018JD029858.

Verlinde, J., and Coauthors, 2007: The Mixed-Phase Arctic Cloud Experiment. *Bull. Amer. Meteor. Soc.*, **88**, 205–222, https://doi.org/10.1175/BAMS-88-2-205.

Walden, V. P., W. L. Roth, R. S. Stone, and B. Halter, 2006: Radiometric validation of the atmospheric infrared sounder over the Antarctic plateau. *J. Geophys. Res.*, **111**, D09S03, https://doi.org/10.1029/2005JD006357.

Weertman, J., 1974: Stability of the junction of an ice sheet and an ice shelf. *J. Glaciol.*, **13**, 3–11, https://doi.org/10.1017/S0022143000023327.

Wilson, A., R. C. Scott, M. P. Cadeddu V. Ghate, and D. Lubin, 2018: Cloud optical properties over West Antarctica from shortwave spectroradiometer measurements during AWARE. *J. Geophys. Res. Atmos.*, **123**, 9559–9570, https://doi.org/10.1029/2018JD028347.

Xu, J.-X., and Coauthors, 2017: Source attribution of Arctic black carbon constrained by aircraft and surface measurements. *Atmos. Chem. Phys.*, **17**, 11 971–11 989, https://doi.org/10.5194/acp-17-11971-2017.

Xu, L., L. M. Russell, R. C. J. Somerville, and P. K. Quinn, 2013: Frost flower aerosol effects on Arctic wintertime longwave cloud radiative forcing. *J. Geophys. Res. Atmos.*, **118**, 13 282–13 291, https://doi.org/10.1002/2013JD020554.

——, ——, and S. M. Burrows, 2016: Potential sea salt aerosol sources from frost flowers in the pan-Arctic region. *J. Geophys. Res. Atmos.*, **121**, 10 840–10 856, https://doi.org/10.1002/2015JD024713.

Zhang, D., A. M. Vogelmann, P. Kollias, E. P. Luke, F. Yang, D. Lubin, and Z. Wang, 2019: Comparison of Antarctic and Arctic stratiform mixed-phase cloud properties using ground-based remote sensing measurements. *J. Geophys. Res. Atmos.*, **124**, 10 186–10 204, https://doi.org/10.1029/2019JD030673.

Zou, X., D. H. Bromwich, J. P. Nicolas, A. Montenegro, and S.-H. Wang, 2019: West Antarctic surface melt event of January 2016 facilitated by foehn warming. *Quart. J. Roy. Meteor. Soc.*, **145**, 687–704, https://doi.org/10.1002/qj.3460.

Zwally, H. J., M. B. Giovinetto, J. Li, H. G. Cornejo, M. A. Beckley, A. Brenner, J. L. Saba, and D. Yi, 2005: Mass changes of the Greenland and Antarctic ice sheets and shelves and contributions to sea-level rise: 1992–2002. *J. Glaciol.*, **51**, 509–527, https://doi.org/10.3189/172756505781829007.